7 DRIP SHIELD AND DYNAMIC ROCK BLOCK IMPACT PERFORMANCE ANALYSES

The U.S. Department of Energy (DOE) is designing the drip shield so it will protect the waste package from direct rock block impacts. This chapter conveys the results obtained from a parametric study that assesses the effects of rock block size and fall height on the ability of the drip shield to mitigate damage to the waste package. The results of this parametric study have been used to develop the abstractions implemented within the MECHFAIL Total-system Performance Assessment (TPA) Version 5.0 beta code module. Specific abstractions developed include the maximum displacement of the drip shield and the plastic strain incurred by the different drip shield components for a given dynamic rock block impact scenario (i.e., rock block size and fall height). In addition, an abstraction that can be used to approximate the drip shield velocity as a function of displacement for a given rock block impact scenario has also been derived. The drip shield velocity-displacement relationship is needed to estimate the potential impact velocity of the drip shield with different waste package sizes in the event the rock block impact scenario is sufficient to cause this type of interaction.

7.1 Finite Element Model Description

The finite element models used to assess the effects of dynamic rock block impacts on the drip shield are consistent with those described in detail in Gute, et al. (2001). As a result, only a brief overview of the finite element models will be presented here.

7.1.1 Drip Shield Finite Element Model

The drip shield and rock block impact finite element model was constructed using two planes of symmetry and plane strain boundary conditions (see Figure 7-1). Note that these boundary conditions are consistent with those used to model the drip shield subjected to static rockfall loads (see Chapter 5) except for the presence of rock rubble along the sides of the drip shield. Rock rubble was not included in the drip shield and rock block impact model because the primary focus of the parametric study was to evaluate the effects of varying rock block sizes and rock block impact velocities (i.e., fall heights) on drip shield performance. If it is determined that dynamic rock block impacts with the drip shield are risk significant, additional analyses can be performed to study the potential beneficial and adverse effects associated with the presence of rock rubble buttressing the drip shield. It is expected that including the presence of rock rubble will reduce the deflection of the drip shield while increasing the likelihood of the Titanium Grade 7 plate being breached for a given rock block impact.

The potential interactions between the drip shield and waste package created by a rock block impact have yet to be evaluated. This study was limited to establishing the possibility of such an occurrence before spending the significant effort that will be required to develop a model that can simulate the event.

Unlike the drip shield and static rockfall load models, the drip shield and dynamic rock block impact models were constructed using eight-noded hexahedral solid elements exclusively. This was necessitated by the use of an explicit, as opposed to an implicit, method of numerical solution to perform the analyses. As a result, reduced integration and hourglassing issues uniquely associated with the explicit numerical technique needed to be taken into consideration.

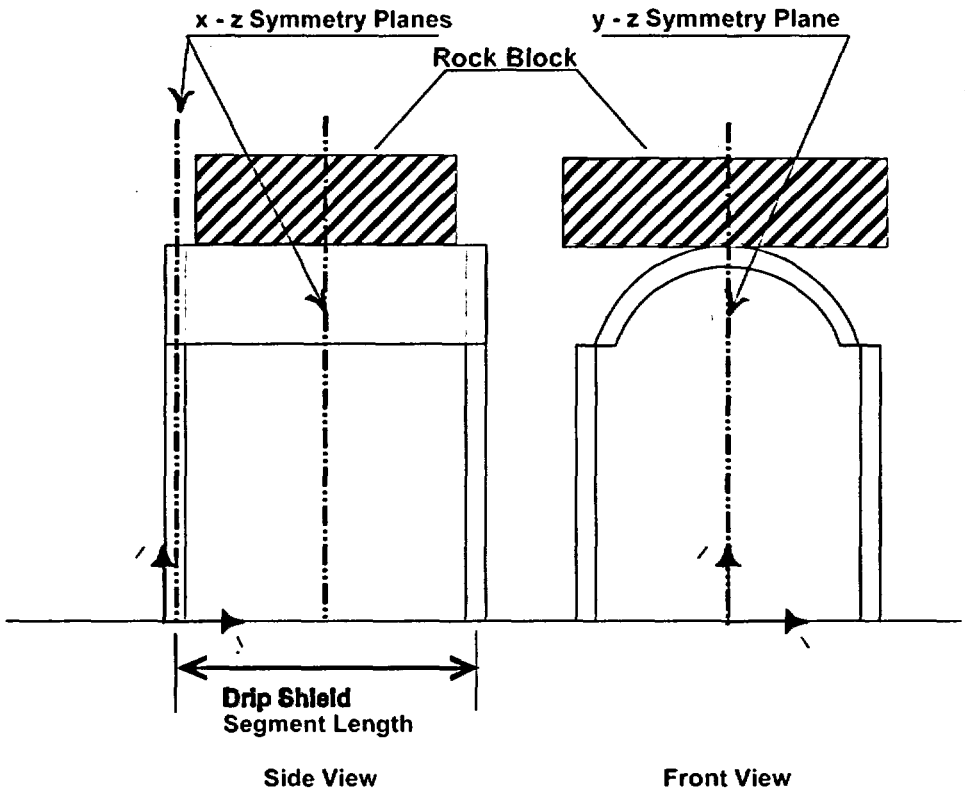

Figure 7-1. Schematic Illustrating the Planes of Symmetry Used to Simplify the Drip Shield and Rock Block Impact Model

Hourglassing occurs because reduced-integration elements consider only the linearly varying part of the incremental displacement field in the element for the calculation of the increment of physical strain. The remaining part of the nodal incremental displacement field is the hourglass field and can be expressed as hourglass modes. Excitation of these modes may lead to severe mesh distortion, with no stresses resisting the deformation. Hourglassing can be avoided by using an adequate mesh density within the model or by introducing artificial numerical damping to suppress the hourglass modes. Because the inappropriate implementation of artificial numerical damping may result in an excessively stiff response by the structure, it was decided that the problem of hourglassing would be addressed by using an adequately refined mesh.

7.1.2 Finite Element Model of the Rock Block

It is generally accepted that the rock block will dissipate some of the energy associated with the impact with the drip shield by localized crushing or fracturing. The amount of energy dissipated through this mechanism is uncertain. Predominant factors that affect the quantity of energy dissipated in this fashion are the magnitude and distribution of stress within the rock block, which are directly dependent on the geometry of the rock block and the ability of the rock block

material to support these stresses without failing (i.e., crushing or fracturing). As presented in earlier progress reports (Gute, et al., 2000, 2001), the rock block has been assumed to have cubic, spherical, or tetrahedron geometries. Moreover, the previous constitutive models for the rock block were either based on the classical metal plasticity model with a von Mises yield surface and perfectly plastic flow rule or the Mohr-Coulomb model cast in terms of the Drucker-Prager yield surface formulation. It is not clear at this time, however, if the development of a rock block finite element model that can reasonably approximate the energy dissipated by crushing or fracturing during the impact event is wholly necessary. Maintaining a constant rock block mass with an infinite material strength during the impact event will, conceptually, provide conservative results because the energy dissipated by crushing or fracturing will not be accounted for. The structural stiffness of the drip shield bulkheads and support beams is, however, likely to be sufficient to cause localized failure of the rock block. This localized failure of the rock block was explicitly accounted for in the construction of the finite element model so the localized shearing of the drip shield plate near the bulkhead would not be underestimated. To accomplish this task, the plane strain boundary conditions were not applied to the face of the rock block whose outward normal is in the negative y-direction (see Figures 7-2a and 7-2b). No other provisions for rock block material or structural failure were taken into consideration within the model (i.e., a simple linear elastic constitutive model was used to represent the mechanical behavior of the rock block mass).

Moreover, the finite element model of the rock block was constructed using the following simplifying assumptions: (i) the rock block is a parallel-piped shape, (ii) the rock block impacts the apex of the drip shield crown with only a vertical component of velocity, and (iii) the rock block is sufficiently long to assume plane strain conditions for the drip shield. Assumption (iii) implies the rock block size should be interpreted as a mass-per-drip-shield segment length. For this study, the drip shield segment length was defined as the distance between two planes bisecting consecutive bulkhead and support beam structural stiffener pairs. The actual drip shield segment length is approximately 1.15 m [3.77 ft].

7.1.3 Finite Element Model Boundary Conditions

7.1.3.1 Loads

A comprehensive discussion of the derivation of the dynamic rock block impact load conditions can be found in Gute, et al. (2001). Table 7-1 summarizes the rock block sizes and impact velocities that were simulated in the parametric study. The combinations of rock block sizes and impact velocities were chosen in the hope of developing simple relationships between the drip shield response and the kinetic energy of the impacting rock block. As the results presented in Sections 7.2 and 7.3 indicate, however, these relationships could not be based on kinetic energy alone. Note that different impact velocities are analogous to different rock block fall heights and are related in Eq. (7-1).

$$v_{rock} = \sqrt{2\,g\,h_{i+1}} \tag{7-1}$$

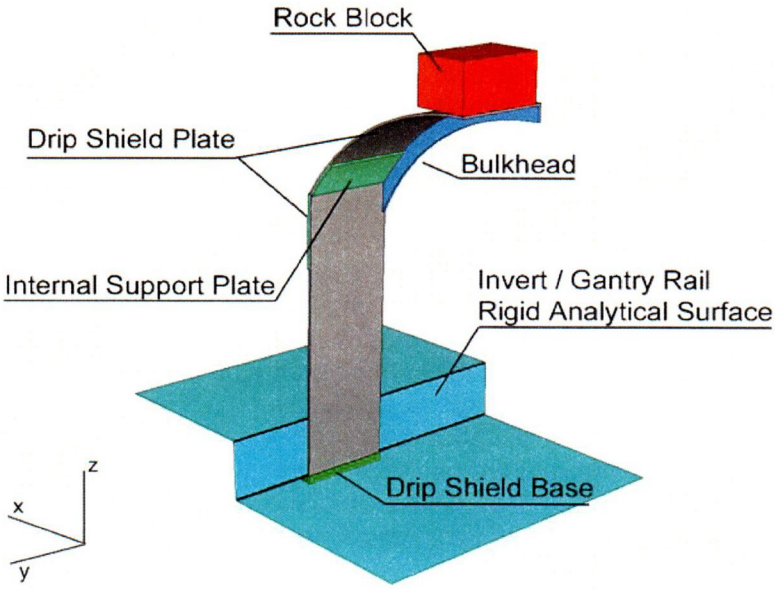

(a)

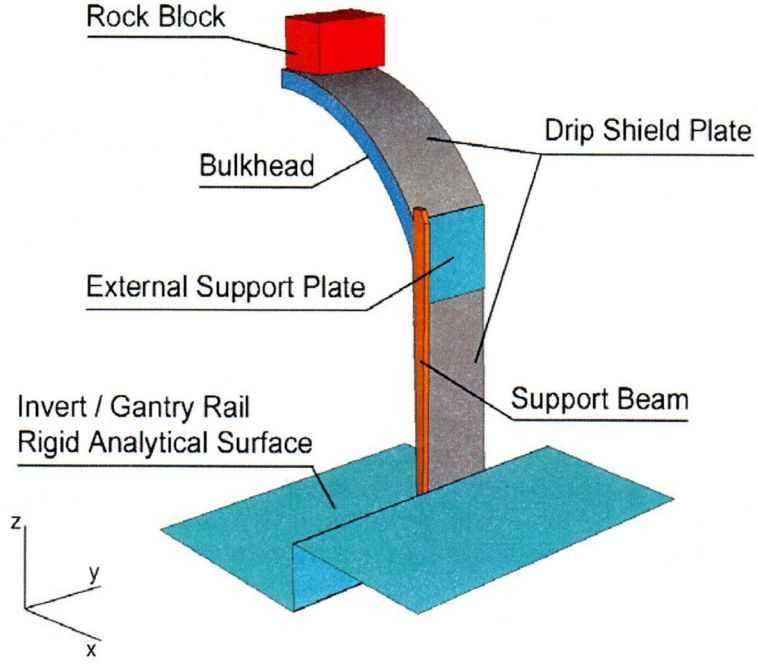

(b)

Figure 7-2. Drip Shield and Rock Block Impact Finite Element Model

Table 7-1. Drip Shield and Rock Block Impact Scenarios Included in the Parametric Study			
Case	Initial Rock Block Impact Velocity, m/s [ft/s]	Rock Block Mass, tonne/m [lb/ft]	Rock Block Impact Kinetic Energy, Joules/m [(ft-lb)/ft]
1	7.0 [23.0]	0.5 [336]	12,250 [2,754]
2	9.9 [32.5]	0.5 [336]	24,500 [5,508]
3	14.0 [45.9]	0.5 [336]	49,000 [11,016]
4	7.0 [23.0]	1.0 [672]	24,500 [5,508]
5	9.9 [32.5]	1.0 [672]	49,000 [11,016]
6	14.0 [45.9]	1.0 [672]	98,000 [22,031]
7	7.0 [23.0]	2.0 [1,344]	49,000 [11,016]
8	9.9 [32.5]	2.0 [1,344]	98,000 [22,031]
9	14.0 [45.9]	2.0 [1,344]	196,000 [44,062]
10	7.0 [23.0]	4.0 [2,689]	98,000 [22,031]
11	9.9 [32.5]	4.0 [2,689]	196,000 [44,062]
12	2.475 [8.12]	4.0 [2,689]	12,250 [2,754]
13	7.0 [23.0]	8.0 [5,378]	196,000 [44,062]
14	1.750 [5.74]	8.0 [5,378]	12,250 [2,754]
15	2.475 [8.12]	8.0 [5,378]	24,500 [5,508]

where

v_{rock} — impact velocity of the rock block (m/s)
g — acceleration due to gravity (m/s^2)
h_{i+1} — rock block fall height (m) (corresponds to the drift degradation zone height at the time the seismic event occurs).

For the current engineered barrier subsystem design (CRWMS M&O, 2000a), it can be shown that the approximate range of potential rock block fall heights is from 2.1 to 9.2 m [6.9 to 30.2 ft]. This range of potential rock block fall heights corresponds to rock block impact velocities from 6.4 to 13.4 m/s [21.1 to 44.1 ft/s]. It should be noted, however, that Eq. (7-1) does not take into consideration the potential for the rock blocks being dislodged from the drift roof with initial velocities induced by the seismic ground motions.

To account for the ground motion associated with the seismic event assumed to be occurring at the same time as the dynamic rock block impact with the drip shield, the drip shield and invert were assumed to be moving at a constant upward velocity of 1 m/s [3.28 ft/s] at the time the impact was initiated. After impact, the invert foundation continued to move upward with a 1-m/s [3.28-ft/s] velocity throughout the duration of the analysis while the drip shield was free to respond to the rock block impact load.

7.1.3.2 Kinematic Constraints

Kinematic constraints are discussed in detail in Gute, et al. (2001) and are illustrated in Figure 7-1. To summarize, the drip shield rock block impact model is simplified by cutting the model by three symmetry planes [see Figures 7-2(a), (b)]. The first two planes are normal to the length axis (y-direction) and cut through the middle of the bulkhead and between the bulkheads. The second plane is normal to the lateral axis (x-direction) and cuts through the center of the drip shield. Nodes that lie on the respective symmetry planes are constrained to those planes. The resultant model represents a continuous drip shield that experiences the rock block impact along its entire length.

Recall from the rock block model discussion in Section 7.1.2 that the rock block was assumed to be fractured at the bulkhead. This assumption will create the shearing condition between the drip shield bulkhead and the drip shield crown plate expected to occur after the rock block was crushed or fractured above the bulkhead. The shear stress calculated in the model should bound any potential shear stress that the drip shield may experience as the result of a rock block impact.

Three different contact interactions were explicitly accounted for in the drip shield and rock block impact model. These were the interactions between the drip shield and the (i) rock block, (ii) supporting invert, and (iii) adjacent gantry rail. A master-slave concept was used within the finite element program to model these interactions. Specifically, the nodes associated with the slave surface cannot penetrate into or through the master surface mesh. The master surface nodes, however, can penetrate through the slave surface. As a consequence, the slave surface mesh should be much more refined than the master surface. Another option was to redundantly define the master-slave relationship—the contact surface pair is defined twice with the surfaces interchanging the master-slave relationship. A redundant master-slave relationship does not allow any nodes from either surface to penetrate through the counterpart surface. Moreover, a redundant master-slave contact definition is only appropriate when the master and slave surfaces have similar mesh densities. Even though the effects of friction can be included as part of the interaction between the two surfaces, the duration and magnitude of the impact load are such that these effects are negligible.

For the case of the drip shield and rock block interaction, the coarsely meshed rock block was used to define the master surface, and the drip shield was the corresponding slave surface. No redundancy was used.

The finite element model also represented the drip shield as a free-standing structure on the invert. In particular, the model employed a friction-free sliding contact boundary condition between the drip shield and the rigid analytical surface to represent the invert and gantry rails (see Figure 7-2). Note that the gantry rail (i.e., the vertical side of the rigid analytical surface) limited the horizontal (x-direction) deflections of the drip shield and provided a potential pivot

point to cause the drip shield to fold up underneath itself (i.e., buckle) if the deformations became sufficiently large.

7.1.4 Finite Element Model Material Properties

See Section 5.1.3 for a summary of the material properties used to develop the constitutive models for the various drip shield components. Gute, et al. (2001) discusses in detail the construction of the bilinear stress-strain curves used to define the elastic-plastic material behavior of the drip shield materials. The specific elastic rock mass material properties used in the drip shield and rock block impact finite element analyses are provided in Table 7-2 (NRC, 2000).

Table 7-2. Elastic Material Properties Used for the Rock Block Mass

Young's Modulus,* GPa [psi]	Poisson's Ratio*
32.6 [4.73×10^6]	0.21

*NRC. "Input to Repository Design and Thermal-Mechanical Effects Issue Resolution Status Report." Rev. 3. Washington, DC: NRC. 2000.

7.2 Summary of Analysis Results

A comprehensive discussion of the general stress and deflection results obtained from the finite element models of the drip shield and rock block impacts can be found in Gute, et al. (2001). That discussion is not repeated here except where it relates directly to the data abstractions presented in Section 7.3.

7.2.1 Drip Shield Deflection

Knowledge of the maximum deflection of the drip shield was required to determine if the drip shield would sufficiently deform under the rock block impact load to strike the waste package. Drip shield deflection was measured by the relative change in gap between the bottom surface of the bulkhead at the apex of the drip shield crown and the top of the waste package. Figures 7-3 through 7-7 show the drip shield deflection history for each load case from Table 7-1.

7.2.2 Drip Shield Component Stresses and Strains

The magnitudes of stress and strain incurred by the drip shield components under dynamic rock block impact loads are required to establish the extent of the damage incurred by the drip shield as a result of this type of event. Figure 7-8 illustrates the regions where maximum stresses and strains occurred within the drip shield plate and bulkhead as the result of dynamic rock block impacts. Table 7-3 provides a summary of the maximum drip shield deflection, drip shield plate and bulkhead von Mises stresses, and drip shield plate and bulkhead equivalent plastic strains that were calculated for each load case.

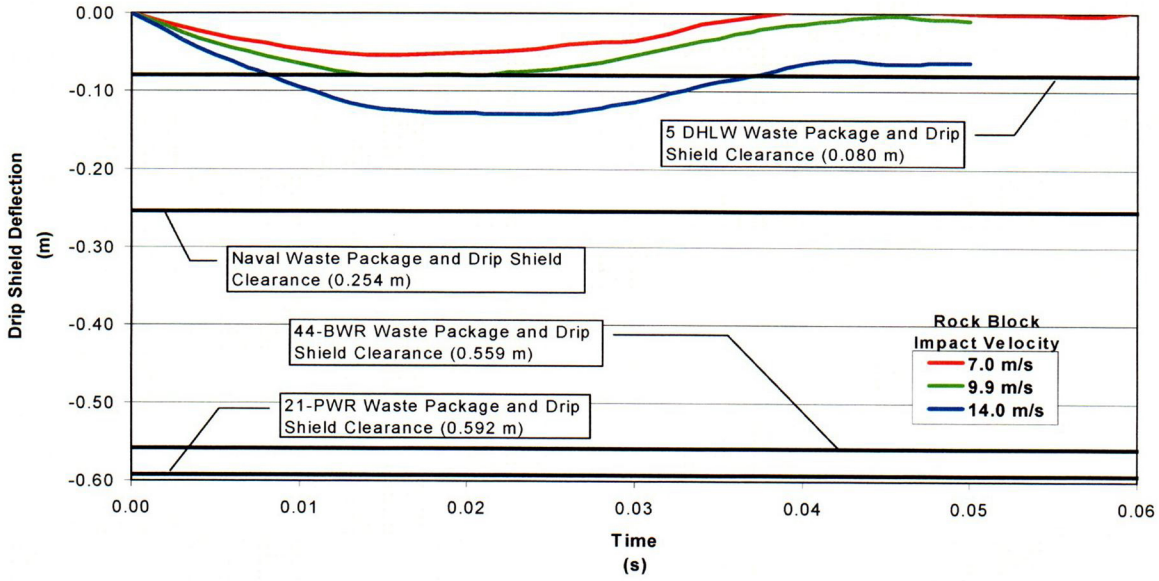

Figure 7-3. Drip Shield Deflection Versus Time for 0.5 tonne/m [336 lb/ft] Rock Block Impacts

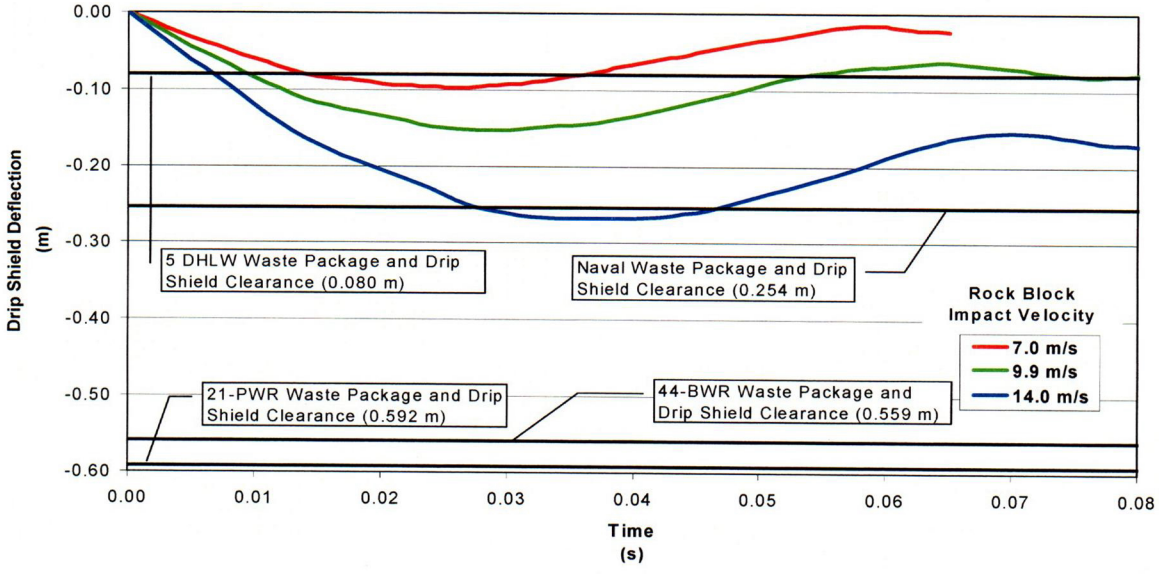

Figure 7-4. Drip Shield Deflection Versus Time for 1.0 tonne/m [672 lb/ft] Rock Block Impacts

C20

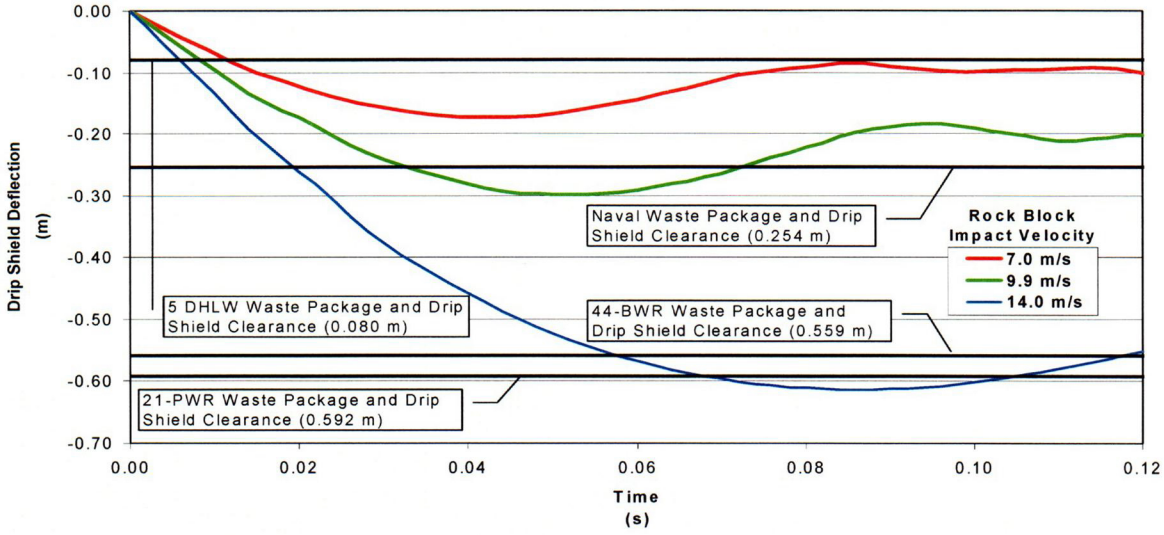

Figure 7-5. Drip Shield Deflection Versus Time for 2.0 tonne/m [1,344 lb/ft] Rock Block Impacts

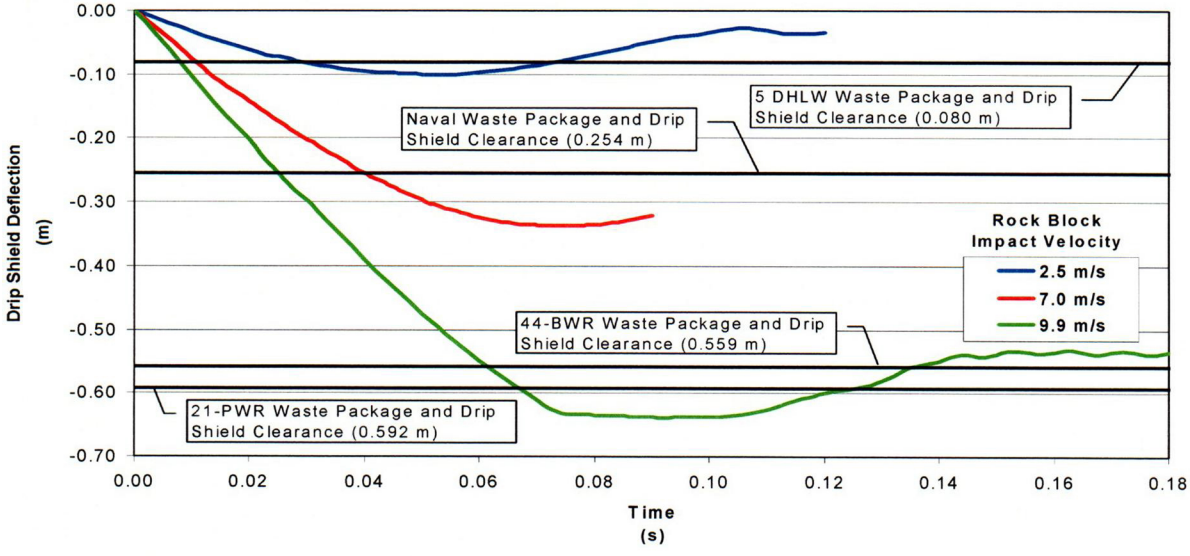

Figure 7-6. Drip Shield Deflection Versus Time for 4.0 tonne/m [2,689 lb/ft] Rock Block Impacts

C21

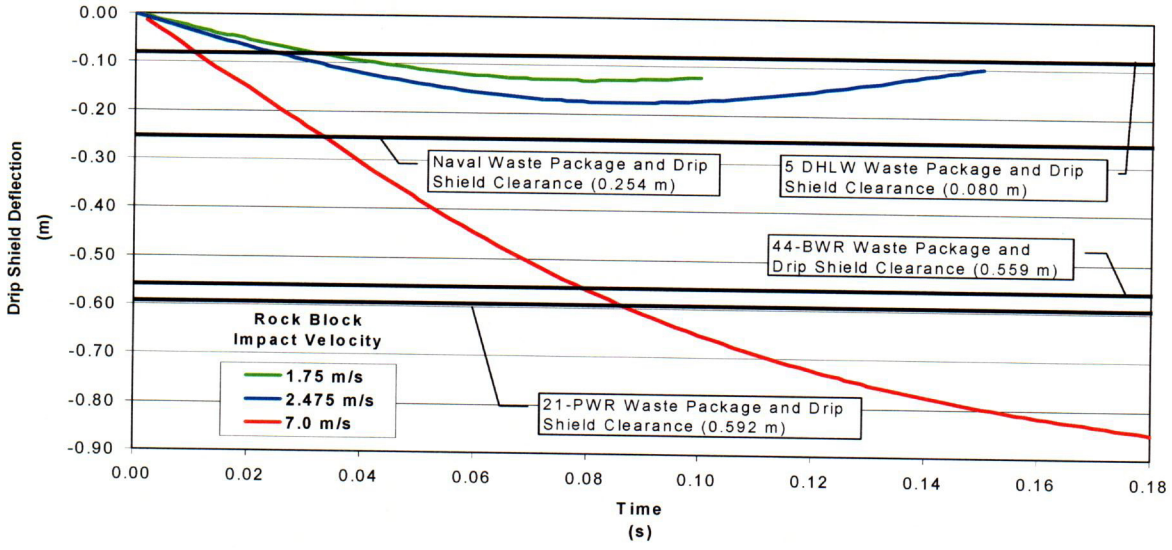

Figure 7-7. Drip Shield Deflection Versus Time for 8.0 tonne/m [5,378 lb/ft] Rock Block Impacts

7.3 Data Abstractions for MECHFAIL

7.3.1 Drip Shield Maximum Deflection Abstraction

The maximum deflection of the drip shield caused by a given rock block impact scenario was assumed to be a function of the rock mass as well as the momentum and kinetic energy of the rock block [see Eq. (7-2)]. The coefficients for Eq. (7-2) were determined using the data obtained from the finite element analyses and the method of Least Squares curve fitting,

$$\delta_{max} \cong \left[7.720 \times 10^{-3}\right] M + \left[3.402 \times 10^{-3}\right] M^2 - \left[3.544 \times 10^{-4}\right] M^3 + \left[1.041 \times 10^{-4}\right] M\, v_{rock} + \left[1.443 \times 10^{-3}\right] M\, v_{rock}^2 \quad (7\text{-}2)$$

where

δ_{max} — maximum drip shield displacement (m)
M — rock block mass (tonne/m)
v_{rock} — rock block impact velocity (m/s)

The normalized error for Eq. (7-2) was calculated using the following relationship

$$\delta_{max}^{err} = \frac{\sum\left[\delta_{max,i} - \delta_{max}\left(M_i, v_{rock,i}\right)\right]^2}{\sum\left[\delta_{max,i}\right]^2} \quad (7\text{-}3)$$

C21A

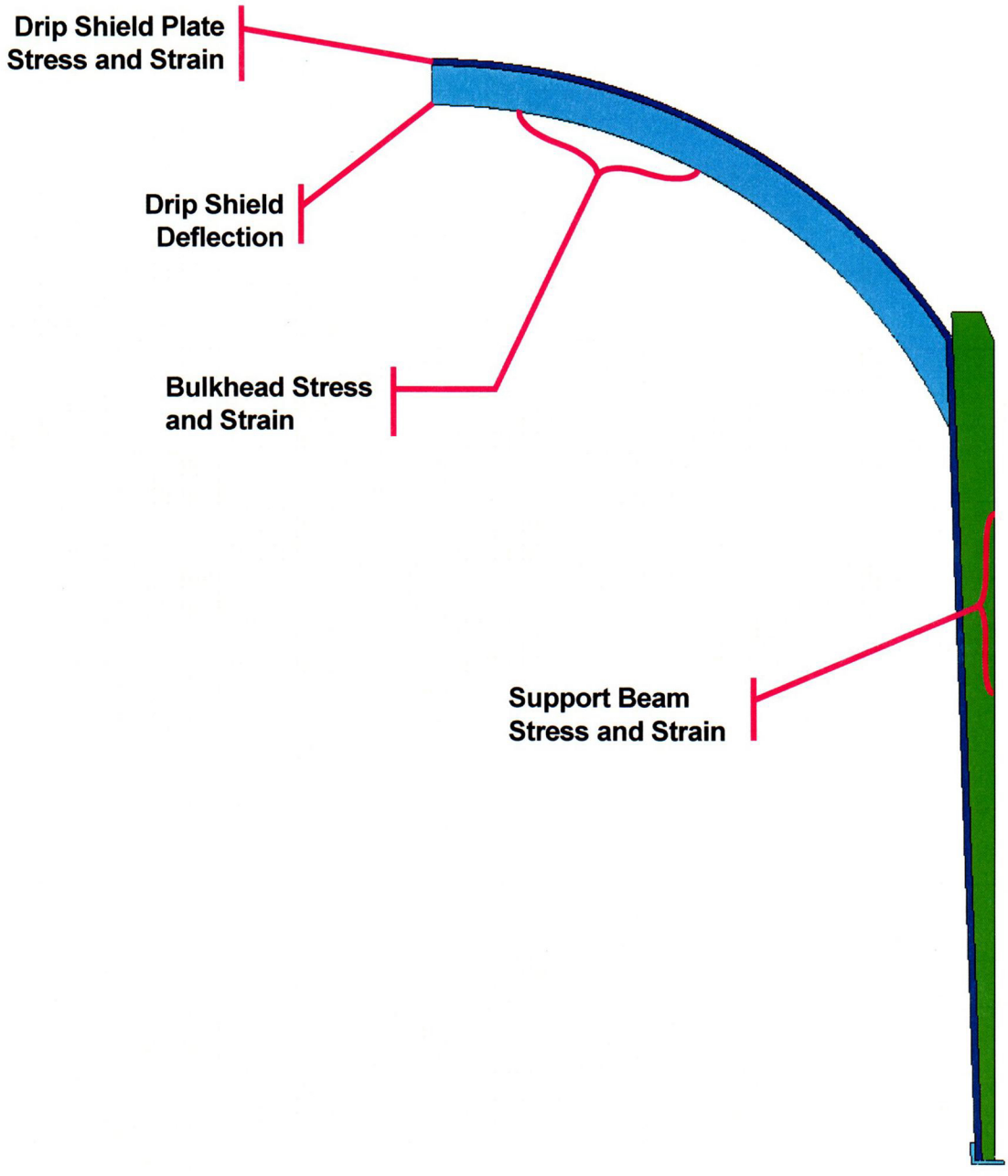

Figure 7-8. General Locations of the Maximum Drip Shield von Mises Stress and Equivalent Plastic Strains

C22

Table 7-3. Maximum Drip Shield Plate and Bulkhead Stress and Strain Results					
		Drip Shield Plate		Drip Shield Bulkhead	
Case	Maximum Drip Shield Deflection, m [ft]	Maximum von Mises Stress, MPa [psi]	Maximum Equivalent Plastic Strain	Maximum von Mises Stress, MPa [psi]	Maximum Equivalent Plastic Strain
1	0.054 [0.177]	176.7 [2.563 × 10^4]	0.004	668.2 [9.691 × 10^4]	0.006
2	0.080 [0.262]	178.1 [2.583 × 10^4]	0.007	685.4 [9.941 × 10^4]	0.015
3	0.130 [0.426]	182.2 [2.643 × 10^4]	0.012	724.6 [1.051 × 10^5]	0.035
4	0.097 [0.318]	212.3 [3.079 × 10^4]	0.054	705.8 [1.024 × 10^5]	0.025
5	0.153 [0.502]	238.0 [3.452 × 10^4]	0.093	737.9 [1.070 × 10^5]	0.047
6	0.268 [0.879]	287.4 [4.168 × 10^4]	0.162	811.9 [1.178 × 10^5]	0.082
7	0.174 [0.571]	260.1 [3.772 × 10^4]	0.124	763.2 [1.107 × 10^5]	0.057
8	0.298 [0.977]	*	*	*	*
9	0.613 [2.011]	*	*	*	*
10	0.338 [1.109]	*	*	*	*
11	0.638 [2,093]	*	*	*	*
12	0.101 [0.331]	207.0 [3.002 × 10^4]	0.047	720.6 [1.045 × 10^5]	0.034
13	*	*	*	*	0
14	0.130 [0.426]	227.4 [3.298 × 10^4]	0.076	741.2 [1.075 × 10^5]	0.044
15	0.175 [0.574]	270.8 [3.928 × 10^4]	0.138	772.6 [1.121 × 10^5]	0.059

*Denotes results that exceeded the material failure criterion and, as a result, were not used to calculate the coefficients of the abstraction formulas.

Using Eq. (7-3), the normalized error for Eq. (7-2) was determined to be

$$\delta_{max}^{err} = 1.77 \times 10^{-3} \tag{7-4}$$

Eq. (7-2) provides a reasonable approximation of the drip shield maximum deflection, δ_{max}, for a limited range of masses, 0.5 [336] $\leq M \leq$ 8.0 tonne/m [5,378 lb/ft], and impact velocities, 1.75 [5.74] $\leq v_{rock} \leq$ 14.0 m/s [45.92 ft/s] (see Figure 7-9). Case 13 from Table 7-1 was not included in the calculation of the coefficients for Eq. (7-2) because no maximum deflection was reached in the finite element analysis. Figure 7-7 clearly shows the drip shield was far from reaching its maximum deflection when the simulation was terminated for this case. In fact, the drip shield appears to be buckling for this particular rock block impact scenario. Figure 7-9 also indicates the drip shield deflection required to cause impacts with some of the different waste package types. A comparison between the abstraction calculation and the finite element data shows that the greatest percentage error occurs in the regime of what can be characterized as low-energy impacts. The magnitude of absolute error, however, shows an excellent correlation to the analysis data. It needs to be emphasized that Eq. (7-2) is only valid within the prescribed data ranges for the rock block mass and impact velocity. This restriction is required because many abstractions use higher order polynomial terms, which will tend to dominate the expression when applied outside the given range.

7.3.2 Drip Shield Displacement and Velocity Relationship Abstraction

The drip shield velocity-displacement relationship was needed to estimate the impact velocity of the drip shield with different waste package sizes in the event the rock block impact scenario was sufficient to cause this type of interaction. The results of Gute, et al. (2001) showed the regions of plastic strain in the drip shield were relatively small, which indicated a limited amount of rock block energy was absorbed by permanent deformation of the drip shield components. This behavior was true for all cases except Case 13, which did not achieve maximum deflection and appears to be buckling. The remaining cases indicated that at maximum drip shield deflection (where velocity of the rock block was zero) the drip shield absorbed the rock block's kinetic and potential energy primarily through elastic deformation. Figures 7-3 through 7-7 support this observation because drip shield deflection versus time follows a generally sinusoidal shape, which is analogous to a simple linear spring and mass system response under similar loading conditions. Therefore, it is assumed that the drip shield and rock block interaction is linear elastic through the point of maximum deflection.

The velocity of the rock block and drip shield crown when it impacts the waste package can be approximated using Eq. (7-5). The data points in Figure 7-10 are normalized for each scenario such that velocity and deflection have a range of zero to one. Equation (7-5) is also normalized and plotted for comparison. This data abstraction provides a bounding solution to the simulation data.

$$V = \left(v_{rock} + 1\right)\left[1 - \left(\frac{C}{\delta_{max}}\right)^2\right]^{1/2} \tag{7-5}$$

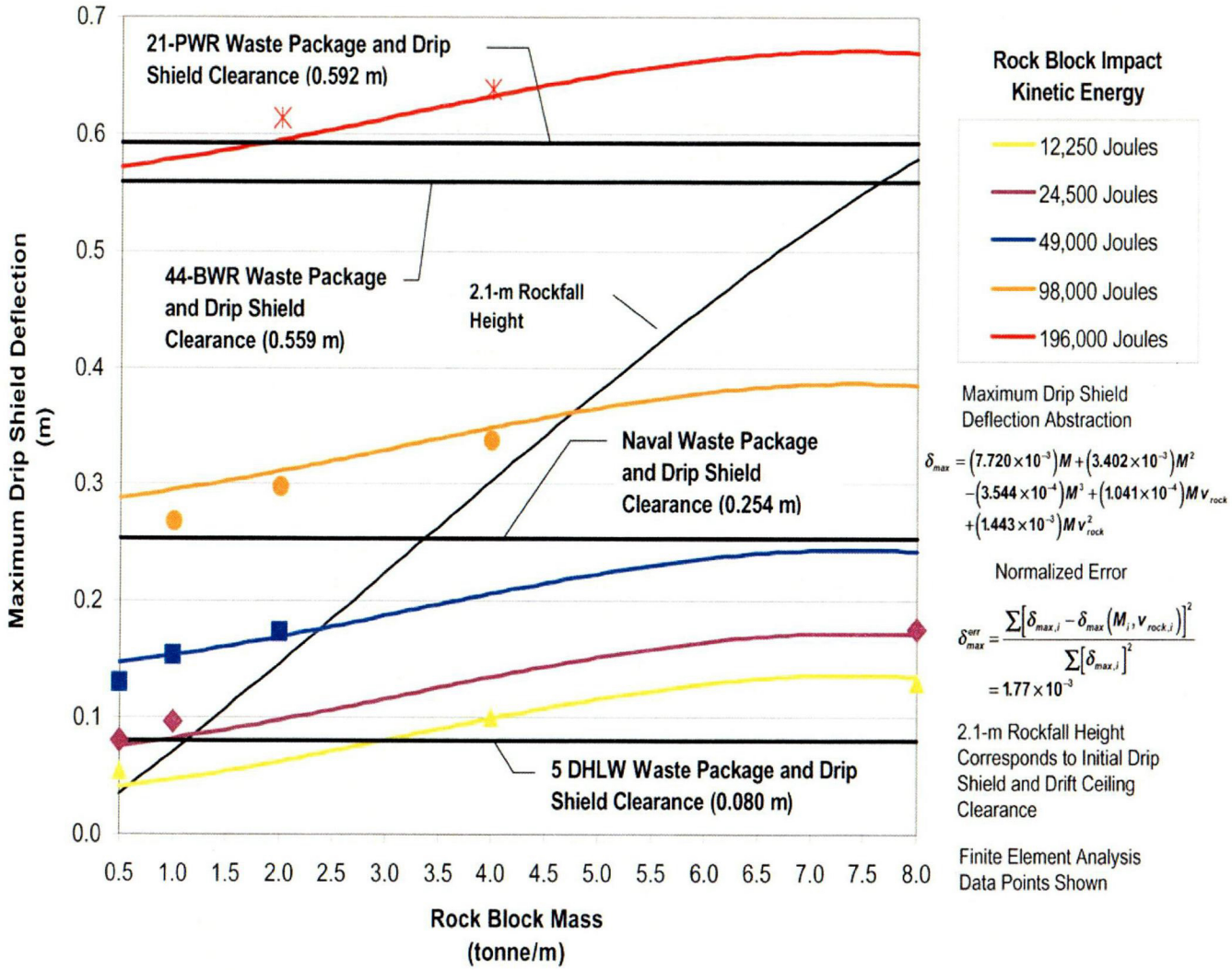

Figure 7-9. Maximum Drip Shield Deflection Abstraction for Rock Block Impacts

C23

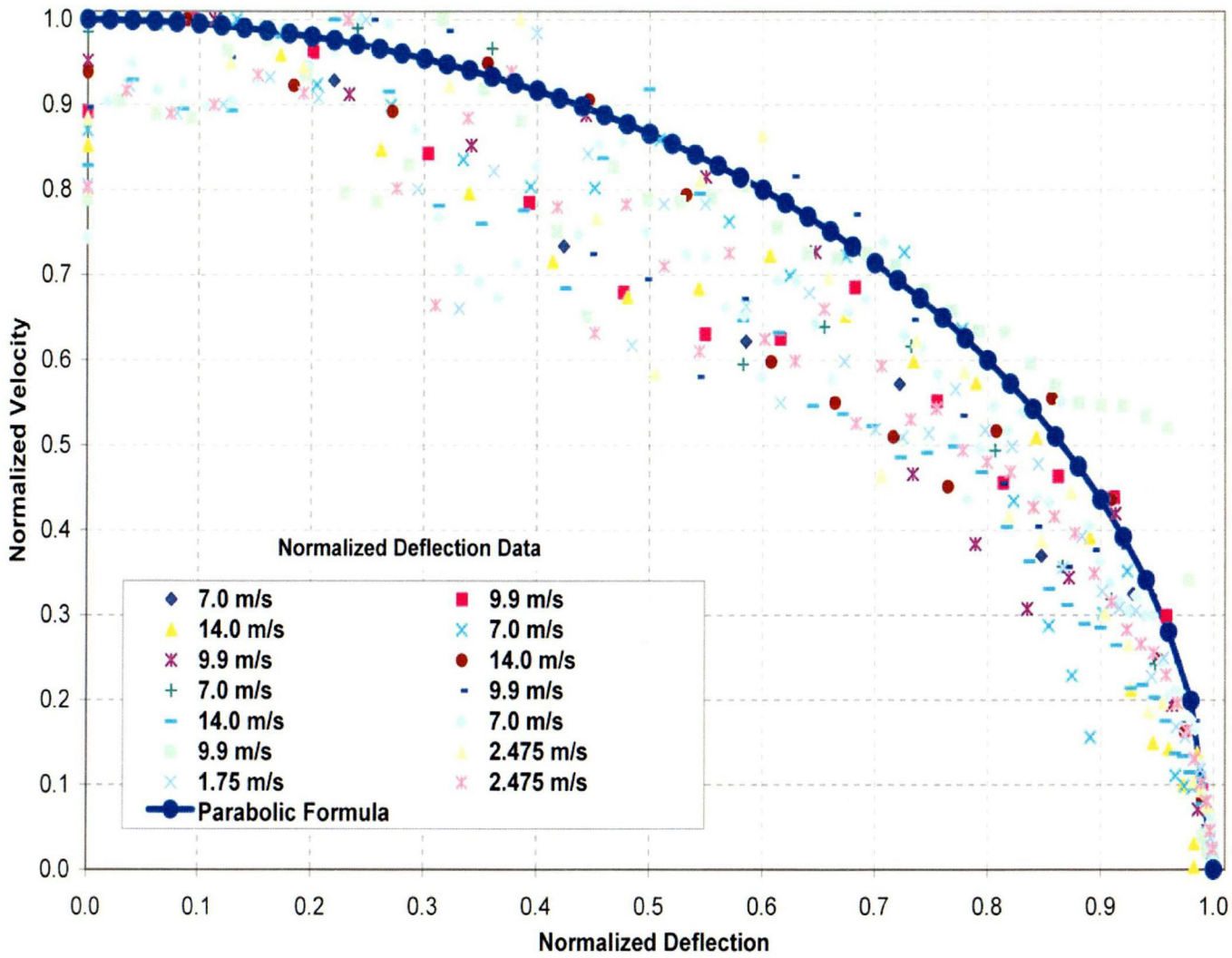

Figure 7-10. Drip Shield Velocity as a Function of Displacement Caused by Rock Block Impacts

C24

where

v	—	drip shield velocity when impacting the waste package (m/s)
v_{rock}	—	initial rock block impact velocity (m/s)
C	—	clearance between the drip shield and waste package prior to the impact event (m), $C < \delta_{max}$
δ_{max}	—	maximum deflection of the drip shield if allowed to deform freely (m)

7.3.3 Drip Shield Component Stress and Plastic Strain Abstractions

The abstractions for the maximum stresses and plastic strains for the drip shield plate and bulkhead under dynamic rock block impact conditions were derived using the data summarized in Table 7-3. No abstractions were developed for the support beam because its response to the rock block impact loads was predominantly linear (i.e., the calculated stresses were well below the yield stress threshold). This observation was not valid for Case 13, however, where the dynamic rock block load was sufficient to cause buckling of the drip shield. This result demonstrates that 8 tonne/m [5,378 lb/ft] rock blocks can deflect the drip shield to the extent that it will impact the waste package, regardless of the initial clearance between them. The 7-m/s [23.0-ft/s] rock block impact velocity corresponds to a rockfall of 2.1 m [6.89 ft], which is the clearance between the drip shield crown and drift roof before any drift degradation occurs. Equations (7-6) through (7-9) are the abstractions that can be used to estimate the maximum stresses and plastic strains for the drip shield plate and bulkhead components in terms of the rock block mass and impact velocity. It is important to recognize, however, that these abstractions are only valid if the drip shield does not interact with the waste package.

$$\sigma_{plate} = \left(1.371 \times 10^{2}\right) - \left(5.889 \times 10^{0}\right) M + \left(9.255 \times 10^{0}\right) M v_{rock} + \left(8.683 \times 10^{-2}\right) M v_{rock}^{2} \quad (7\text{-}6)$$

$$\sigma_{bulkhead} = \left(6.419 \times 10^{2}\right) + \left(3.052 \times 10^{0}\right) M + \left(4.366 \times 10^{0}\right) M v_{rock} + \left(5.306 \times 10^{-1}\right) M v_{rock}^{2} \quad (7\text{-}7)$$

$$\varepsilon_{plate} = -\left(5.229 \times 10^{-2}\right) - \left(8.765 \times 10^{-3}\right) M + \left(1.338 \times 10^{-2}\right) M v_{rock} + \left(1.156 \times 10^{-4}\right) M v_{rock}^{2} \quad (7\text{-}8)$$

$$\varepsilon_{bulkhead} = -\left(7.877 \times 10^{-3}\right) + \left(1.195 \times 10^{-3}\right) M + \left(2.447 \times 10^{-3}\right) M v_{rock} + \left(2.766 \times 10^{-4}\right) M v_{rock}^{2} \quad (7\text{-}9)$$

where

σ_{plate}	—	maximum von Mises stress for the drip shield plate (MPa)
$\sigma_{bulkhead}$	—	maximum von Mises stress for the drip shield bulkhead (MPa)
ε_{plate}	—	maximum equivalent plastic strain for the drip shield plate (m/m)
$\varepsilon_{bulkhead}$	—	maximum equivalent plastic strain for the drip shield bulkhead (m/m)

Using the normalized error relationship defined in Eq. (7-3), the normalized error for the drip shield component von Mises stress and equivalent plastic strain abstractions were determined to be

$$\sigma_{\text{plate}}^{\text{err}} = 2.15 \times 10^{-3}$$

$$\sigma_{\text{bulkhead}}^{\text{err}} = 4.10 \times 10^{-5}$$

$$\varepsilon_{\text{plate}}^{\text{err}} = 2.74 \times 10^{-2}$$

$$\varepsilon_{\text{bulkhead}}^{\text{err}} = 3.78 \times 10^{-3}$$

The results from Cases 8, 9, 10, 11, and 13 were not included in the derivation of Eqs. (7-6) through (7-9). These cases were excluded because the maximum von Mises stress exceeded the failure stress (i.e., ultimate tensile strength) for these particular scenarios. Once the failure stress of a material has been exceeded, the material behaves as an elastic-perfectly plastic material (i.e., the material loses the ability to carry any additional stress while accumulating additional plastic strain). This change in material behavior introduced a severe discontinuity in the calculated stress and strain values. The accuracy of the abstractions for those loading conditions that did not cause the drip shield component materials to exceed the failure criteria would be adversely affected if the results from Cases 8, 9, 10, 11, and 13 were included in the derivation of Eqs. (7-6) through (7-9). Furthermore, attempting to capture post-failure stress and strain behavior of the drip shield component materials does not serve any practical engineering purpose.

Figures 7-11 through 7-14 illustrate how well the drip shield plate and bulkhead abstractions for the maximum von Mises stress and plastic strain correlate with the results obtained from the finite element models. These figures also convey the relationship of the abstracted results with the component material yield stress and ultimate tensile strength.

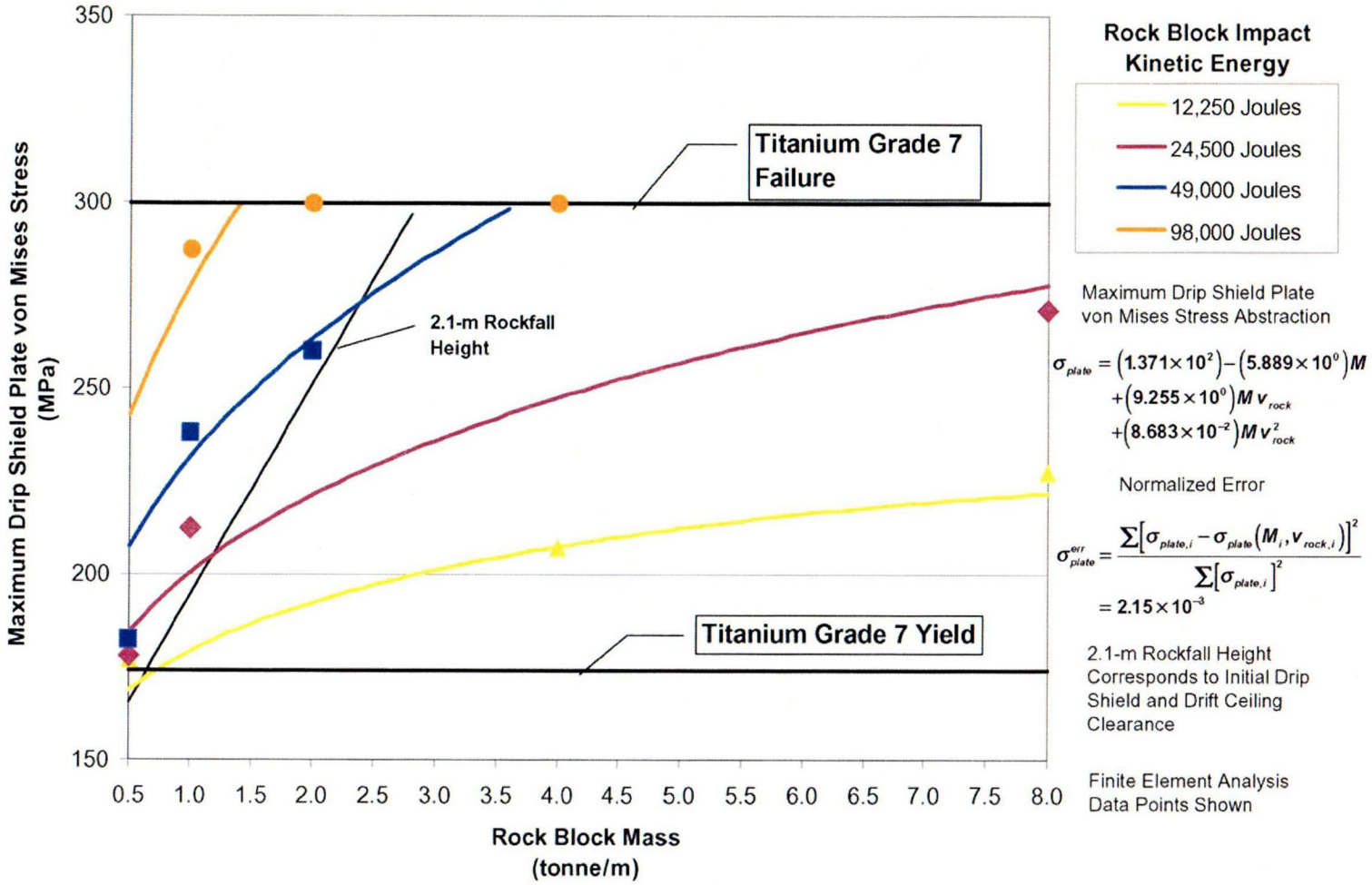

Figure 7-11. Maximum Drip Shield Plate von Mises Stress Abstraction for Rock Block Impacts

C25

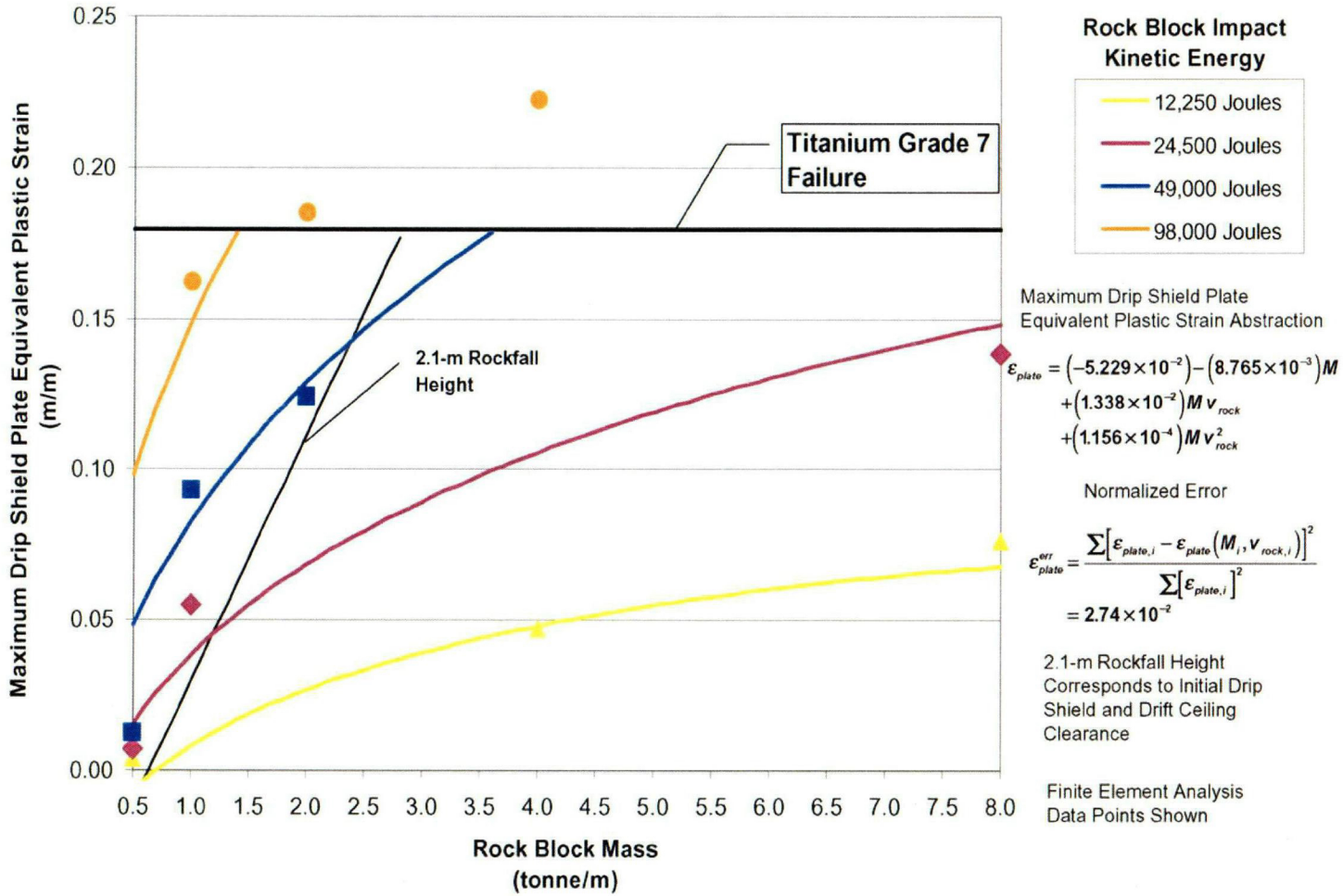

Figure 7-12. Maximum Drip Shield Plate Equivalent Plastic Strain Abstraction for Rock Block Impacts

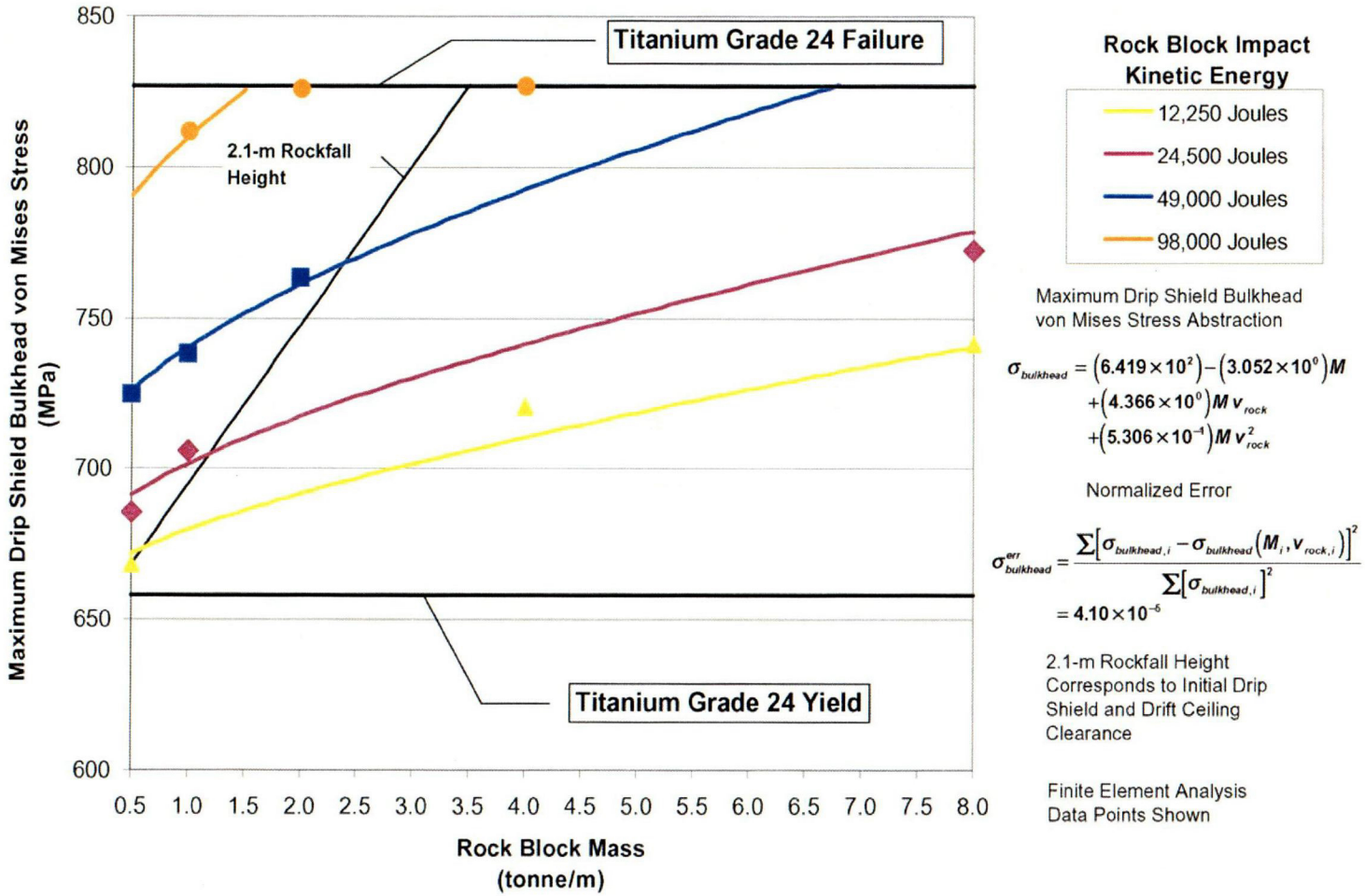

Figure 7-13. Maximum Drip Shield Bulkhead von Mises Stress Abstraction for Rock Block Impacts

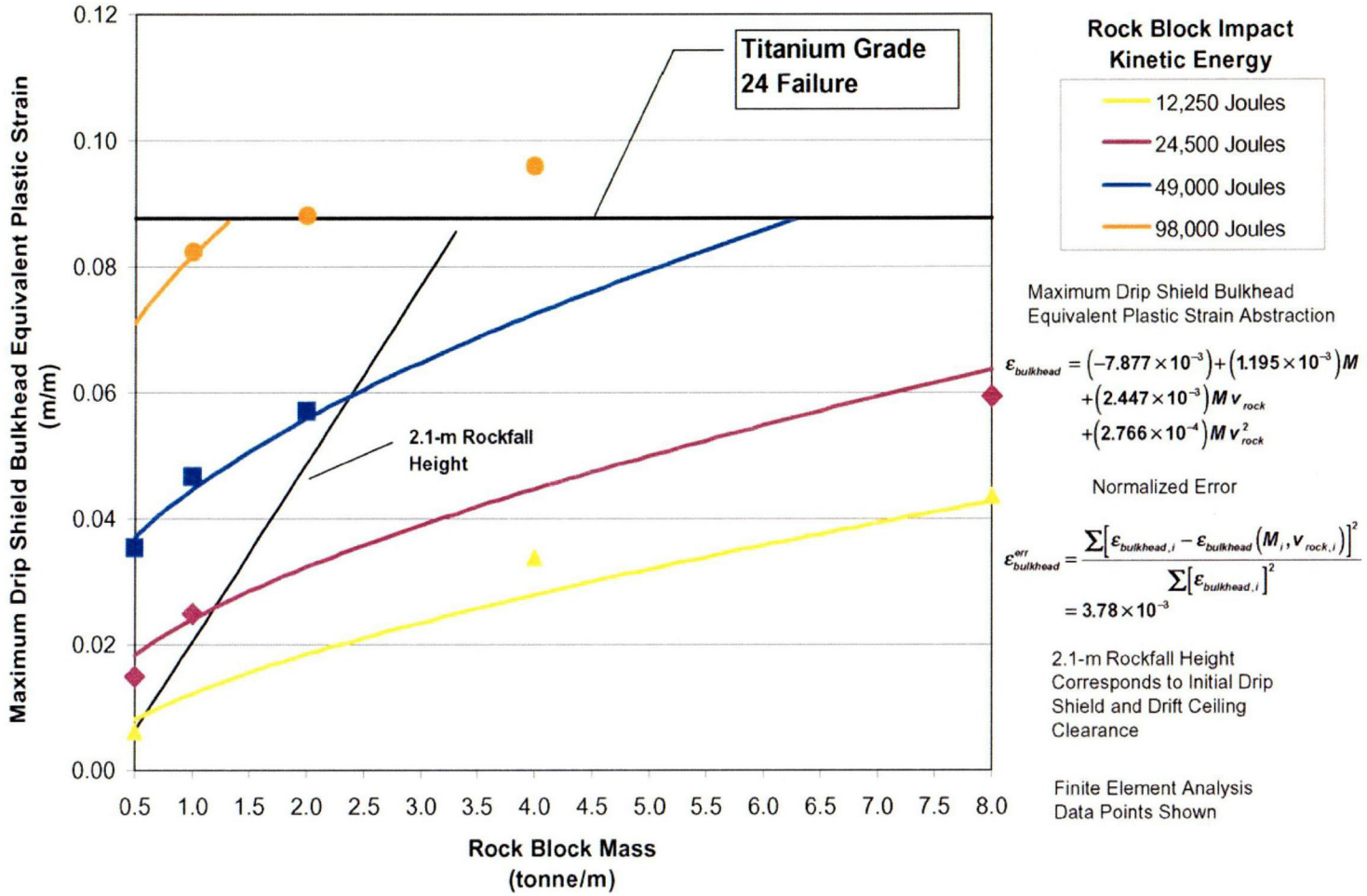

Figure 7-14. Maximum Drip Shield Bulkhead Equivalent Plastic Strain Abstraction for Rock Block Impacts

C28

8 SEISMIC PERFORMANCE ANALYSES

It is expected that the proposed Yucca Mountain geologic repository will be subjected to earthquakes of varying magnitudes throughout the entire 10,000-yr regulatory period. As a result, an understanding of the response of the various components of the engineered barrier subsystem components—including the drip shield, waste package, waste form, pallet, invert, and drift—to these earthquake loads, as well as potential interactions between them, need to be understood. This chapter documents the work accomplished thus far in achieving this goal. Specifically, the methodology used to approximate the natural frequencies and mode shapes of the drip shield are provided in Section 8.1.

Natural frequencies and mode shapes of a structure provide insight as to how the structure will behave when subjected to time-varying loading conditions. Although the discussion in this chapter focuses on seismic ground motions, time varying impact loads are also of interest [e.g., dynamic rock block impacts (see Chapter 7)]. Theoretically, impact loads will excite all the natural frequencies of the impacted structure. In practice, however, the magnitude, orientation, and duration of the impact load play significant roles in determining which of the natural frequencies of the structure will govern its response. In the case of seismically generated ground motions, only those natural frequencies below 33 Hz for a given structure, system, or component are generally excited during an earthquake. The 33-Hz threshold was established by analyzing seismic ground motion measurements of actual earthquakes from around the world over several decades. These analyses demonstrated that earthquakes do not have any appreciable energy content at frequencies above 33 Hz. In fact, the American Society of Civil Engineers Standard ASCE 4-98 (American Society of Civil Engineers, 1999) indicates that the base shear for cantilever models with uniform mass distribution may be determined using the equivalent-static-load method. That is, if the fundamental natural frequency of the structure is high enough, typically 33 Hz or above, such that dynamic amplification will not occur, the zero period acceleration of the floor may be used to approximate the base shear of the cantilever model.

8.1 Approximation of Drip Shield Natural Frequencies

The undamped natural frequencies and mode shapes of the drip shield are of interest for various kinematic constraint conditions. Accumulated rockfall rubble on the top and sides of the drip shield and its effects on the natural frequencies and mode shapes of the drip shield are also scenarios that need to be investigated. The scope of the discussion presented here, however, is limited to how the drip shield natural frequencies and mode shapes were approximated using the finite element method without the effects of accumulated rockfall.

8.1.1 Drip Shield Finite Element Model Description

Sections 8.1.1.1–8.1.1.3 convey the rationale and technical bases for the various assumptions and boundary conditions implemented in the construction of the finite element model used to approximate the drip shield natural frequencies and mode shapes. Section 8.1.1.4 presents a summary of the results obtained from the drip shield natural frequency and mode shape analyses.

8.1.1.1 Drip Shield Finite Element Model Geometry

Figure 8-1 represents the finite element model geometry used to approximate the drip shield natural frequencies and mode shapes. The model was constructed using a mixture of plate and solid elements. Plate elements were used for the Titanium Grade 7 panel sections; including the drip shield crown, side plates, and inner and outer stiffening plates. Plate elements were also used to represent the Alloy 22 base of the structure. Solid hexahedron elements were used to represent the major structural support beam and bulkhead components. The total geometry approximated a complete drip shield structure (CRWMS M&O, 2000a, Reference Sketch Number SK-0148, Revision 05). To adequately approximate potential lateral and twisting mode shapes and their concomitant natural frequencies, geometric symmetry was not used to reduce the overall size of the drip shield finite element model. In addition, the effects of nonsymmetric boundary conditions could be investigated when using a full-scale model.

Linear material behavior and small strains and displacements are assumed when approximating the natural frequencies and mode shapes of a given structure. As a result, the use of plate elements to represent thin structural members, such as the Titanium Grade 7 plate regions, was justified. The ability to use plate elements in the construction of the drip shield finite element model significantly reduced the memory requirements and computational times required to perform the analyses relative to a model composed solely of solid elements.

All of the drip shield natural frequencies less than 50 Hz and their concomitant mode shapes were calculated using the finite element method of approximation.

8.1.1.2 Drip Shield Finite Element Model Boundary Conditions

8.1.1.2.1 Loads

No external loads, including gravity loads, were applied to the drip shield because it is a free-standing structure. The potential effects on the drip shield structural stiffness created by gravity loads have minimal influence on the approximated natural frequencies and mode shapes of the structure. Future analyses may be performed to assess the potential effects of accumulated rockfall rubble on the drip shield natural frequencies and mode shapes. Accumulated rockfall may affect both the effective mass and stiffness of the drip shield.

8.1.1.2.2 Kinematic Constraints

Three types of constraints were applied to the base of the drip shield to assess their effects on the natural frequencies and mode shapes of the structure. These constraints were referred to as free, lateral, and cantilever constraint conditions. The free constraint refers to the condition where the drip shield is allowed to translate and rotate freely in all directions. This condition provides insight into the combined effects of structural stiffness and mass distribution on the dynamic behavior of the drip shield structure. The free constraint condition represents the conditions that will exist in the drift after the gantry crane rails have corroded to a state where they no longer laterally constrain the transverse motion of the drip shield.

The lateral constraint limits translation at the base of the drip shield to axial and vertical motion only. In other words, the two sides of the drip shield base are not allowed to translate

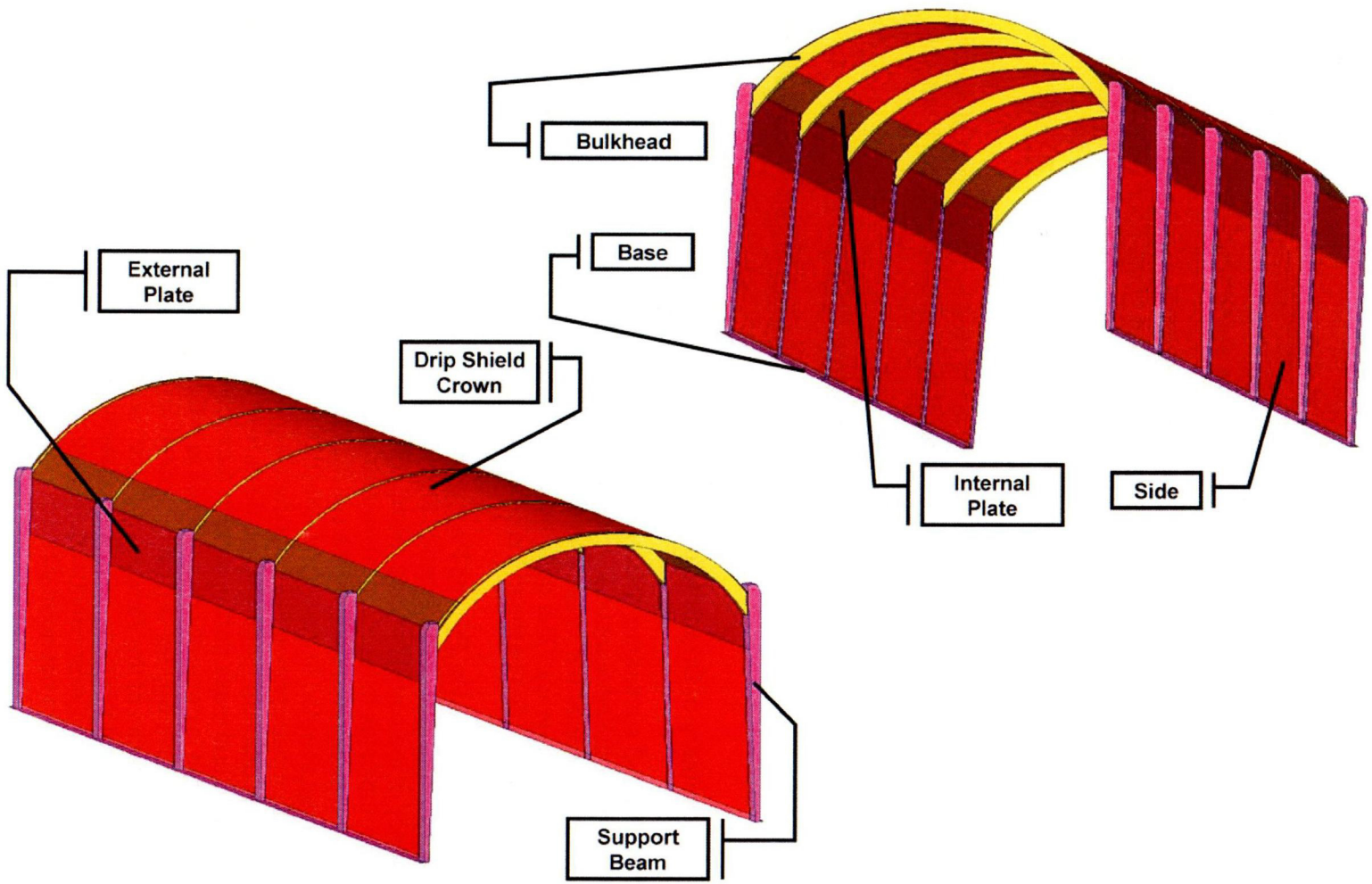

Figure 8-1. Model Used to Approximate the Drip Shield Natural Frequencies and Mode Shapes

side-to-side, neither closer together nor further apart, but are only free to translate within parallel planes. Moreover, no rotational restrictions are applied at the base of the drip shield for the lateral constraint condition. The lateral constraint condition physically represents the restricted motion of the drip shield base created by the presence of the gantry crane rails on the exterior of the drip shield and the waste package on its interior. The lateral constraint condition best represents the current engineered barrier subsystem and subsurface facility design. Figure 8-2 shows the base of the drip shield was constrained in the lateral x-direction.

The cantilevered constraint condition represents a completely constrained drip shield base. This constraint is similar to the base being bolted or clamped to the floor. Figure 8-3 shows the bottom edges of the drip shield are constrained in all six degrees of freedom (i.e., the three translational and three rotational degrees of freedom). The cantilevered constraint was included in the investigation to address the possibility of the U.S. Department of Energy anchoring the drip shield to the invert.

Because each drip shield unit is loosely connected to the next by way of a post and slot configuration (CRWMS M&O, 2000a), the two ends of the drip shield did not have any constraints applied to them.

8.1.1.3 Drip Shield Finite Element Model Material Properties

The material properties used for the different drip shield components are documented in Section 5.1.3.

8.1.1.4 Summary of Drip Shield Natural Frequencies and Mode Shapes

Tables 8-1 through 8-3 summarize the drip shield natural frequencies and their corresponding mode shapes and modal participation factors for each of the three kinematic constraint conditions described earlier (i.e., free, lateral, and cantilevered). The Mode number indicates the order sorted by frequency. The data, however, are sorted by shape to facilitate the comparison of similar modes between the different constraint conditions.

Modal participation factors Px, Py, and Pz provide a relative measure of the directional response of a structure that is subjected to an excitation which has a frequency at, or near, the natural frequency of the corresponding mode. For example, a large Py, relative to Px and Pz for the given mode, indicates that an excitation with a frequency near the mode's natural frequency oriented in the y-direction will likely cause significant deformations of the structure. Conversely, the same excitation oriented in the x- or z-direction will cause structural deformations that are much smaller than those created in the y-direction. Modal participation factors can also be compared between different mode shapes because modal participation factors are related to the amount of structural mass participating in the motion. The ease with which two different modes can be excited is generally proportional to the magnitude of each mode's directional participation factor. This way Px can be compared for one mode shape with Pz in another. As an example, an excitation of the same energy (i.e., a hammer strike) would more easily excite the x-direction of Lateral Wall Zero (Px) with a lateral constraint than the z-direction of Lateral Wall One (Pz) with a cantilever constraint. Note that the participation factors presented in Tables 8-1 through 8-3 are not normalized to unity.

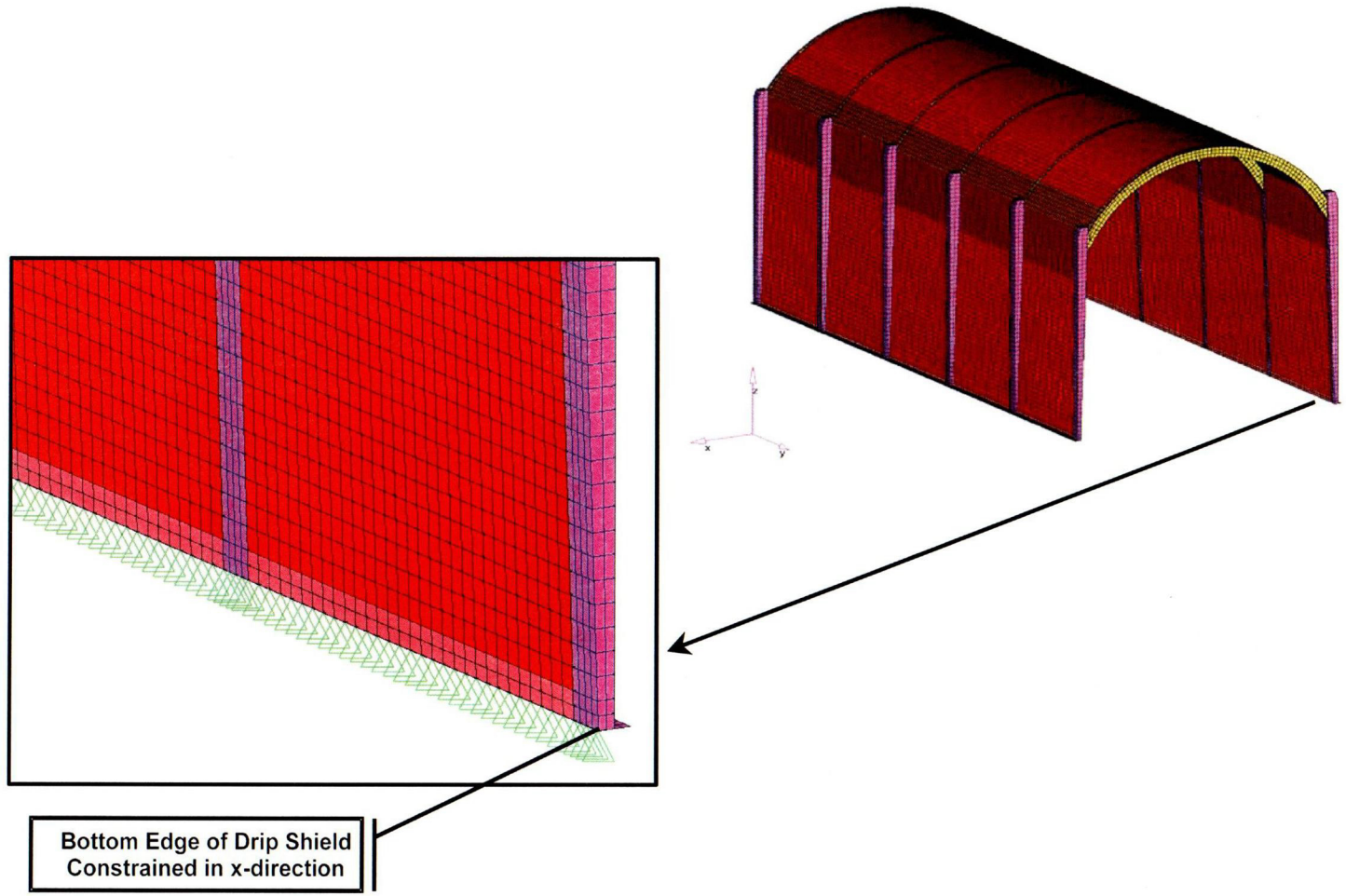

Figure 8-2. Illustration of the Drip Shield Lateral Constraint Condition

C30

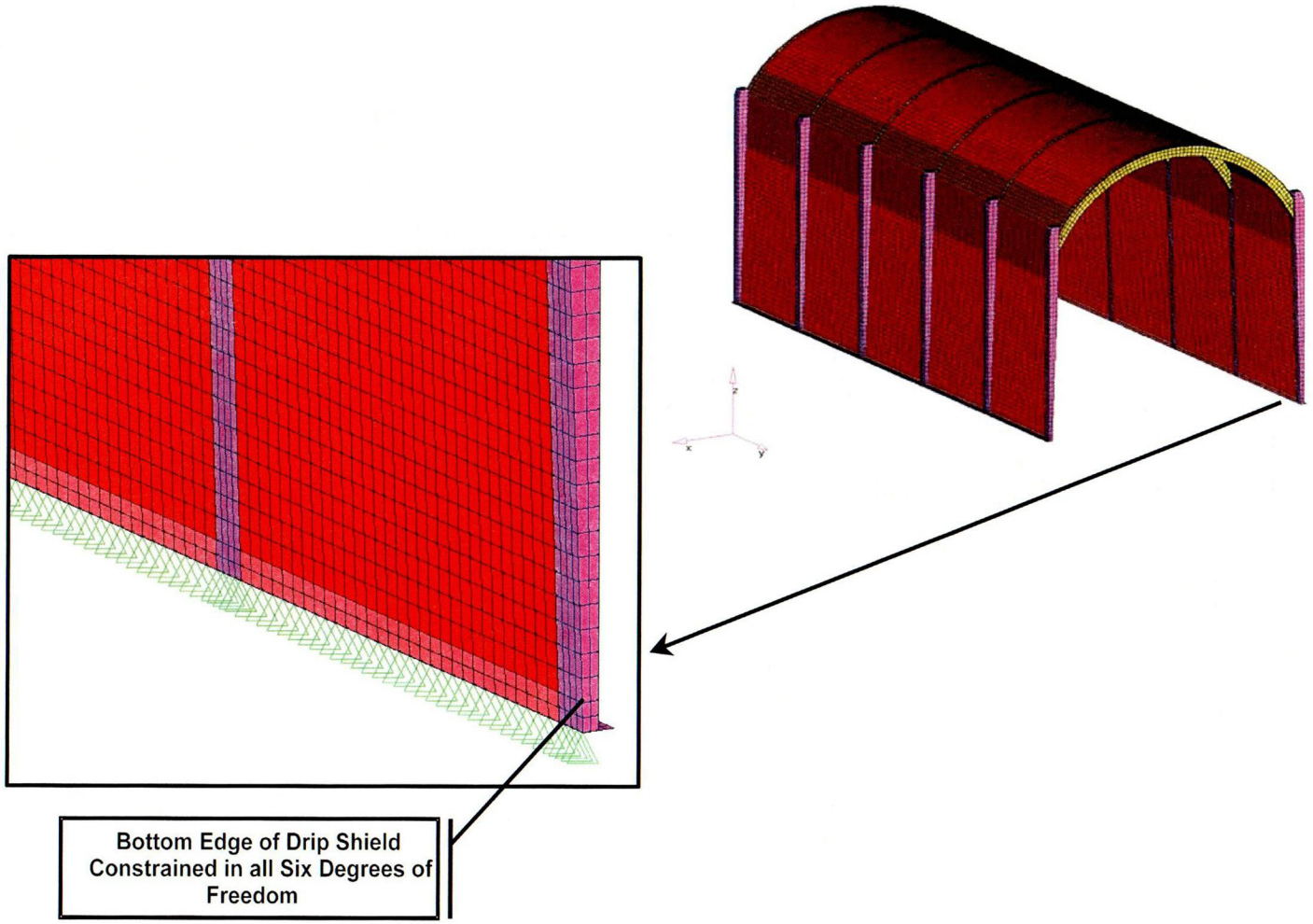

Figure 8-3. Illustration of the Drip Shield Cantilevered Constraint Condition

C31

Table 8-1. Mode Shapes, Natural Frequencies, and Modal Participation Factors of the Drip Shield for Free Constraint Conditions					
Mode Shape Designation	Mode Number	Frequency, Hz	Modal Participation Factors		
			Px	Py	Pz
Free Rigid Body Modes	1–6	0	—	—	—
Walking	7	2.5	4.7×10^{-10}	8.4×10^{-12}	3.3×10^{-10}
Walk with Twist One	—	—	—	—	—
Vertical Up/Down	—	—	—	—	—
Flapping Zero	8	5.9	-1.6×10^{-9}	4.7×10^{-12}	-4.5×10^{-11}
Flapping One	9	7.2	-1.3×10^{-12}	6.2×10^{-11}	5.8×10^{-12}
Flapping Two	10	15.4	-1.7×10^{-10}	8.9×10^{-12}	-2.9×10^{-11}
Flapping Three	14	23.1	-1.9×10^{-11}	1.7×10^{-12}	4.0×10^{-13}
Flapping Four	18	34.5	-2.0×10^{-11}	-1.2×10^{-12}	3.0×10^{-12}
Lateral Wall Zero	—	—	—	—	—
Lateral Wall One	—	—	—	—	—
Lateral Wall Two—Mid	11	14.6	-1.4×10^{-10}	5.7×10^{-12}	7.0×10^{-13}
Lateral Wall Two—Mid	12	16.2	-2.3×10^{-10}	3.7×10^{-12}	-2.3×10^{-11}
Lateral Wall Two—End	13	16.6	3.6×10^{-11}	-4.3×10^{-12}	-3.5×10^{-12}
Lateral Wall Three	15	23.5	5.6×10^{-12}	4.1×10^{-12}	1.2×10^{-12}
Lateral Wall Four—Mid	17	33.9	5.1×10^{-12}	6.6×10^{-13}	-4.3×10^{-13}
Lateral Wall Five—Mid	20	45.1	-1.6×10^{-12}	3.5×10^{-14}	5.3×10^{-13}
Pinch Crown Zero	16	31.6	-6.4×10^{-11}	-1.9×10^{-12}	5.7×10^{-12}
Pinch Crown One	19	34.8	9.3×10^{-12}	3.9×10^{-12}	1.7×10^{-12}

Table 8-2. Mode Shapes, Natural Frequencies, and Modal Participation Factors of the Drip Shield for Lateral Constraint Conditions					
Mode Shape Designation	Mode Number	Frequency, Hz	Modal Participation Factors		
			Px	Py	Pz
Free Rigid Body Modes	1–4	0	—	—	—
Walking	5	1.5	7.7×10^{-10}	-9.1×10^{-10}	6.8×10^{-10}
Walk with Twist One	7	9.1	1.3×10^{-10}	-4.4×10^{-12}	-3.3×10^{-11}
Vertical Up/Down	6	8.7	5.1×10^{-1}	-2.3×10^{-12}	2.8×10^{-11}
Flapping Zero	—	—	—	—	—
Flapping One	—	—	—	—	—
Flapping Two	—	—	—	—	—
Flapping Three	—	—	—	—	—
Flapping Four	—	—	—	—	—
Lateral Wall Zero	—	—	—	—	—
Lateral Wall One	10	37.7	6.6×10^{-1}	1.2×10^{-12}	-3.3×10^{-12}
Lateral Wall Two—Mid	11	39.0	7.6×10^{-2}	-3.0×10^{-13}	-2.5×10^{-13}
Lateral Wall Two—Mid	12	39.4	1.5×10^{-9}	-1.4×10^{-10}	-2.7×10^{-13}
Lateral Wall Two—End	13	40.0	5.5×10^{-1}	-7.1×10^{-13}	-6.9×10^{-13}
Lateral Wall Three	14	45.4	-2.2×10^{-7}	8.8×10^{-13}	-2.4×10^{-13}
Lateral Wall Four—Mid	—	—	—	—	—
Lateral Wall Five—Mid	—	—	—	—	—
Pinch Crown Zero	8	21.9	-2.3×10^{-4}	1.5×10^{-12}	-5.9×10^{-12}
Pinch Crown One	9	23.8	-3.7×10^{-12}	7.2×10^{-12}	-1.7×10^{-12}

Table 8-3. Mode Shapes, Natural Frequencies, and Modal Participation Factors of the Drip Shield for Cantilever Constraint Conditions					
Mode Shape Designation	Mode Number	Frequency, Hz	Modal Participation Factors		
			Px	Py	Pz
Free Rigid Body Modes	0	0	—	—	—
Walking	—	—	—	—	—
Walk with Twist One	—	—	—	—	—
Vertical Up/Down	—	—	—	—	—
Flapping Zero	—	—	—	—	—
Flapping One	—	—	—	—	—
Flapping Two	—	—	—	—	—
Flapping Three	—	—	—	—	—
Flapping Four	—	—	—	—	—
Lateral Wall Zero	1	7.3	1.0×10^{-4}	-5.0×10^{-11}	-3.7×10^{-1}
Lateral Wall One	4	46.7	8.9×10^{-1}	1.5×10^{-7}	2.9×10^{-2}
Lateral Wall Two—Mid	—	—	—	—	—
Lateral Wall Two—Mid	—	—	—	—	—
Lateral Wall Two—End	—	—	—	—	—
Lateral Wall Three	—	—	—	—	—
Lateral Wall Four—Mid	—	—	—	—	—
Lateral Wall Five—Mid	—	—	—	—	—
Pinch Crown Zero	2	26.7	-4.0×10^{-11}	-1.6×10^{-1}	-1.1×10^{-11}
Pinch Crown One	3	28.6	-1.1×10^{-8}	-7.4×10^{-3}	1.7×10^{-8}

Figures 8-4 through 8-7 illustrate the various mode shapes listed in Tables 8-1 through 8-3. There are no mode shapes associated with rigid body modes. The free rigid body modes, as the name implies, are motions along unconstrained directions. Therefore, the free constraint condition has six rigid body modes because the structure is free to translate along the x-, y-, and z-axes as well as rotate about the x-, y-, and z-axes. Similarly, the lateral constraint has the effect of preventing x-axis translation and y-axis rotation. As a result, the lateral constraint condition has four rigid body modes. Finally, the cantilever constraint prevents any rigid body motions (i.e., no rigid body modes).

Walking mode shapes (see Figure 8-4) are characterized by the left and right sides of the drip shield moving forward on the right and aft on the left or vice versa. The visual effect is that the drip shield appears to be walking.

Before describing the remaining mode shape types, it is necessary to discuss what is meant by the order of these modes. Orders are included in the shape name starting at zero and increasing incrementally. Each order is an indication of the number of bends in the shape. For example, a zero order mode has no bends and represents a generally flat shape. An order of one indicates a simple arc shape while an order of two indicates an s-shape and so on. Specific features of each mode shape are described below and illustrated in Figures 8-5 through 8-7.

Flapping modes (see Figure 8-5) and lateral wall modes (see Figure 8-6) are very similar. They are both characterized by motion of the side walls but contrast in the deflection of the opposing wall. Flapping modes, as the name implies, have the appearance of the side walls flapping (i.e., the opposing wall motions are moving 180 degree out of phase with each other). In other words, the side walls deflect away or toward each other at the same moment. The lateral wall mode shapes, on the other hand, are dominated by motions wherein the opposing walls move in unison in the lateral direction (i.e., the opposing wall motions are in phase with each other). More succinctly, if the left wall moves laterally to the left, then the right wall also moves left and vice versa. It should also be noted that there are multiple lateral wall two mode shapes. It is quite common for natural frequency extraction analyses to calculate multiple shapes of the same basic pattern. Multiple mode shapes occur in the drip shield because the basic s-shape for the lateral wall two mode can have several permutations with the change of inflection occurring within different drip shield segments.

The pinch crown mode shapes (Figure 8-7) are similar to the flapping mode shapes except that the deformed shape is characterized by significant bending of the bulkhead and drip shield crown. In addition, the maximum deformation occurs above the drip shield base rather than on the base.

As expected, the natural frequencies of each of the constraint conditions were generally higher as kinematic constraints were added. However, this was not always the case between similar mode shapes. The natural frequency actually reduced for the two pinch crown mode shapes from the free to lateral constraint conditions. While the lateral constraint condition increased the drip shield's structural stiffness, this constraint condition also increased the mass participation along the direction of motion. The natural frequency was reduced for the pinch crown mode shapes because the increase in mass participation was greater than the increase in stiffness when changing from a free to lateral constraint condition.

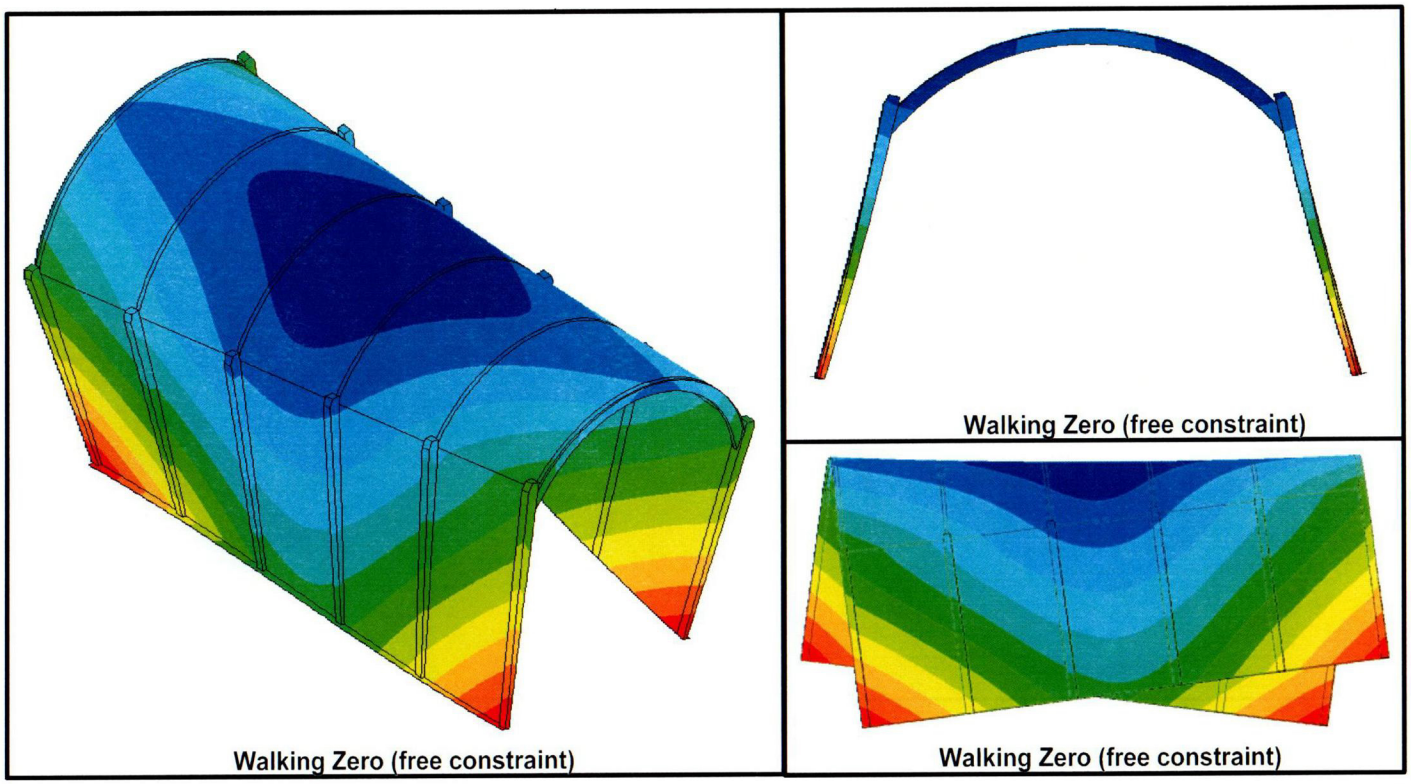

Contour colors represent relative deflection magnitude.

Figure 8-4. Illustration of the Drip Shield Walking Mode Shape

C32

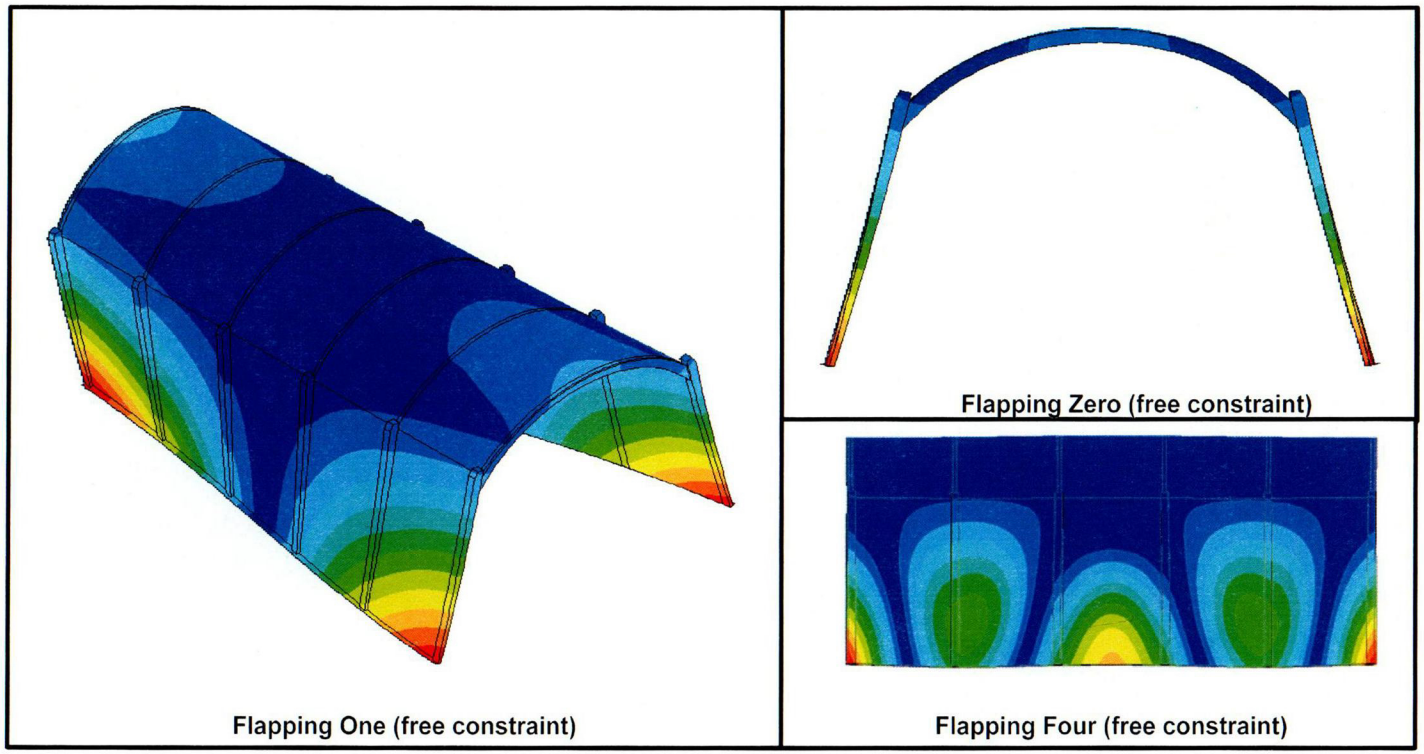

Contour colors represent relative deflection magnitude.

Figure 8-5. Illustration of the Drip Shield Flapping Mode Shape

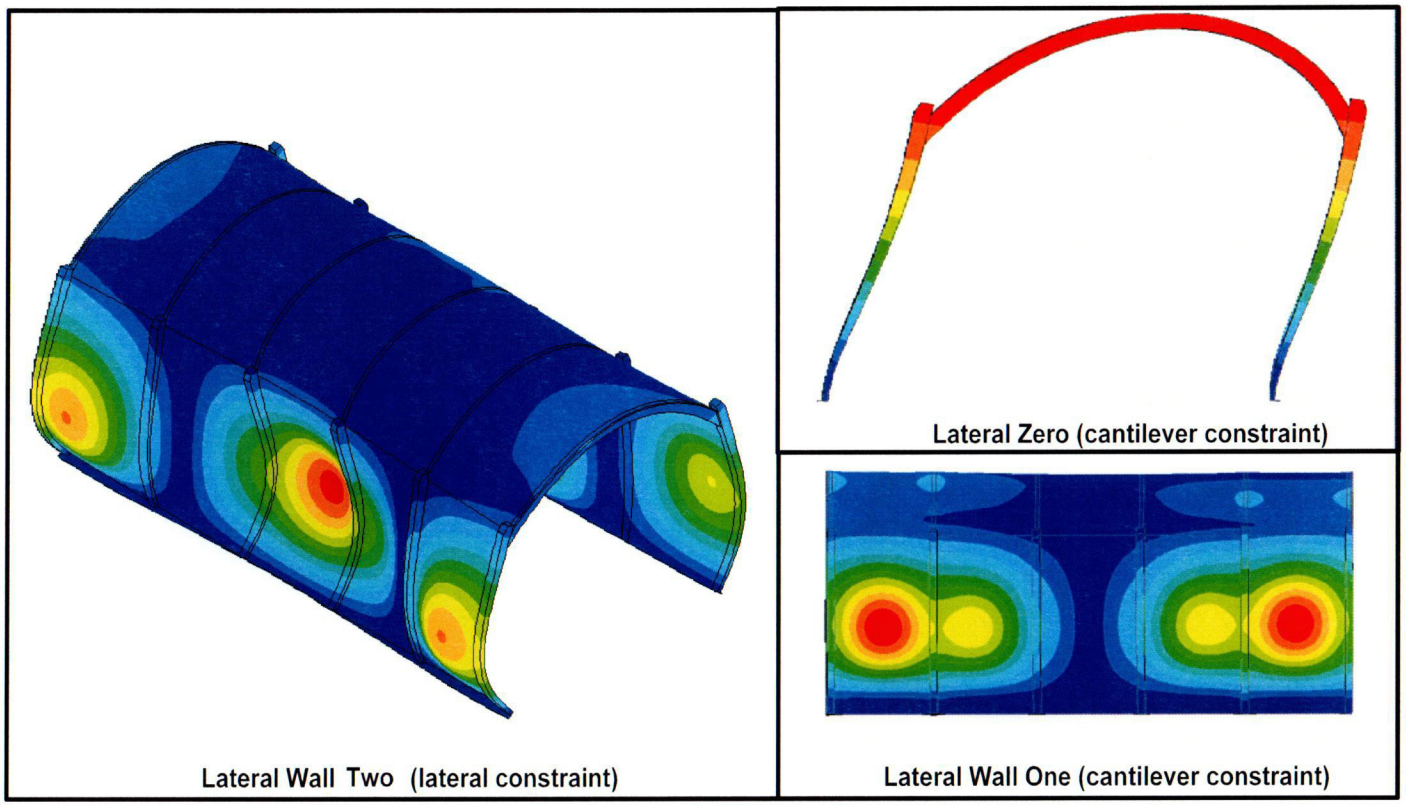

Contour colors represent relative deflection magnitude.

Figure 8-6. Illustration of the Drip Shield Lateral Wall Mode Shape

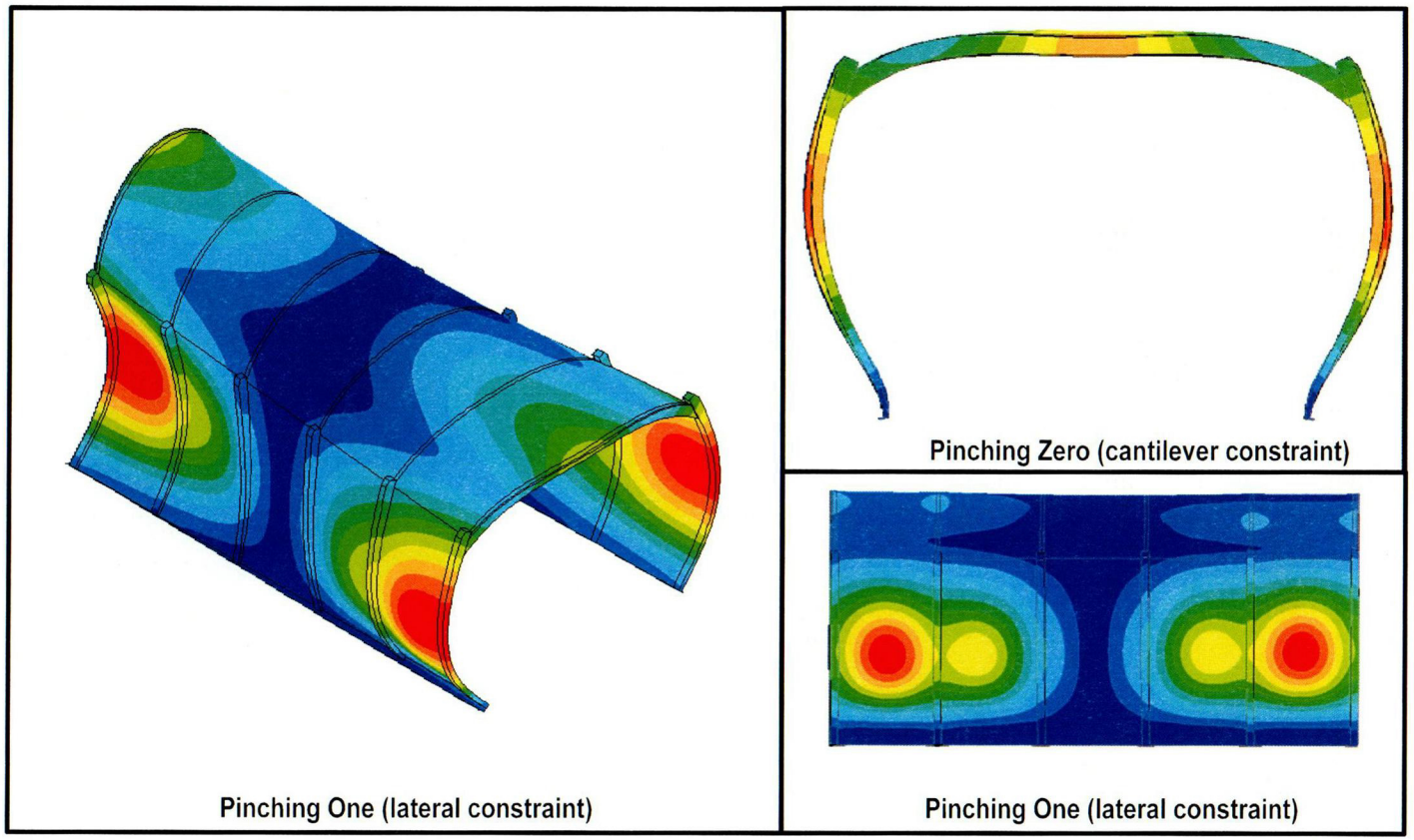

Contour colors represent relative deflection magnitude.

Figure 8-7. Illustration of the Drip Shield Pinch Crown Mode Shape

C35

The natural frequencies and mode shapes presented in Tables 8-1 through 8-3 clearly indicate that the type of constraint applied to the drip shield structure will have a significant influence on how the drip will respond to seismic excitations. For example, the number of modes within the frequency range of a seismic event (i.e., less than or equal to 33 Hz) tended to decrease as additional constraints were added. In the case of the drip shield, the free constraint has 10 mode shapes, the lateral constraint has 5 mode shapes, and the cantilevered constraint has 3 mode shapes that were excited by frequencies less than 33 Hz. None of the 10 free constraint condition mode shapes exhibited a modal participation factor that would be considered to be more dominant than the others. The modal participation factors for the lateral constraint condition, however, indicate that two of the five mode shapes of interest can be considered to be more dominant for excitation frequencies below 33 Hz. These mode shapes are the Lateral Wall Zero and Pinch Crown Zero. Both of these mode shapes respond to excitation in the x-direction. All three of the mode shapes below 33 Hz for the cantilever constraint condition (i.e., Lateral Wall Zero, Pinch Crown Zero, and Pinch Crown One modes) have a relatively high modal participation factor in either the y- or z-direction (i.e., lateral or vertical direction).

Because the drip shield is emplaced as a free-standing structure in the current design of the engineered barrier subsystem, it is not clear how significant higher order effects caused by impact loads arising from the drip shield literally bouncing off of the invert foundation or waste package might be during an earthquake. The work described in the following section attempts to address this issue. The approximated effects of rock block impacts with the drip shield during an earthquake were discussed in Chapter 7.

8.2 Response of the Drip Shield to Seismic Excitations

This work has yet to be completed.

8.2.1 Finite Element Model Description

This work has yet to be completed.

8.2.2 Summary of Analysis Results

This work has yet to be completed.

8.2.3 Data Abstractions for MECHFAIL

This work has yet to be completed.

8.3 Approximation of Waste Package Natural Frequencies

This work has yet to be completed.

8.3.1 Finite Element Model Description

This work has yet to be completed.

8.3.2 Summary of Analysis Results

This work has yet to be completed.

8.4 Response of the Waste Package to Seismic Excitations

This work has yet to be completed.

8.4.1 Finite Element Model Description

This work has yet to be completed.

8.4.2 Summary of Analysis Results

This work has yet to be completed.

8.4.3 Data Abstractions for MECHFAIL

This work has yet to be completed.

9 SUMMARY OF RESULTS

The framework for a new Total-system Performance Assessment (TPA) code module (MECHFAIL) designed to assess the effects of mechanical loading (i.e., static and dynamic rockfall loads and seismicity) on the engineered barrier subsystem was presented in Chapter 2. Specific components of the engineered barrier subsystem presently included in the MECHFAIL failure assessment are the drip shield, waste package, and drift. Potential failure mechanisms of the drip shield that have been accounted for include accumulated equivalent plastic strains that exceed the allowable ductility of the drip shield materials (i.e., the Titanium Grade 7 plates and Titanium Grade 24 bulkheads) attributable to dynamic rock block impacts and creep caused by static rockfall loads. The potential for drip shield buckling under static rockfall loads and seismic excitation are included as well. Although the abstractions have yet to be completed, the MECHFAIL module includes placeholders for assessing drip shield and waste package damage caused by direct seismic shaking and interactions with each other under static and dynamic rockfall loads.

As with the drip shield, the damage incurred by the waste package outer barrier will be characterized in terms of the accumulated equivalent plastic strain. The von Mises stress of the waste package outer barrier will also be evaluated to facilitate the assessment of stress corrosion cracking as a potential failure mechanism.

Failure of the drift by way of thermal, mechanical, hydrological, and chemical degradation processes was accounted for using a time-based drift degradation rate. In addition, the effects of seismic events on drift degradation were explicitly included in the MECHFAIL module. The time varying aspects of drift degradation were correlated with the accumulation of static rockfall loads and occurrence of dynamic rockfall loads acting on the drip shield.

The seismic hazard curve implemented within the TPA code was updated (see Chapter 3) to reflect new information for low annual frequency of occurrence ground motions that was presented by DOE at a recent public meeting.[1] The updated information was added to the mean peak horizontal ground acceleration hazard data provided by CRWMS M&O (1999d). The seismic hazard curve data was derived from probabilistic hazard analyses for fault displacement and vibratory ground motion at Yucca Mountain for a hypothetical rock outcrop reference location [i.e., Point 'A' as defined by the U.S. Geological Survey (1998)]. The seismic hazard curve presented in Figure 3-1 applies to this hypothetical location. Information recently presented by the DOE[2] indicates that the subsurface repository horizon design basis ground motions are likely to be consistent with the Yucca Mountain free surface ground motions attenuated by a factor somewhere in the range of 0.7 to 1.0, depending on the frequency range of interest. To ensure the potential effects of seismicity on repository performance are adequately captured in the TPA code, an attenuation factor of 1.0 is used. The seismic hazard curve in the low annual frequency of exceedance regime (i.e., less than 10^{-6}/yr) has yet to be finalized.[3]

---

[1]DOE and NRC Public Meeting August 6–8, 2002. Las Vegas, Nevada. 2002.

[2]Ibid.

[3]Stepp, C.C. and I.G. Wong. "Probabilistic Seismic Hazard Analysis for Yucca Mountain." Presentation to the Nuclear Waste Technical Review Board February 24, 2003. DOE. Las Vegas, Nevada. 2003.

The approach taken to consider the spatial and temporal variability of static and dynamic rockfall loads within the TPA code was presented in Chapter 4. For an elliptical drift degradation geometry and bulking factors within the range of 1.15 to 1.5, it was demonstrated that the static rockfall loads are likely to lie somewhere in the range of 40 to 160 tonne/m [26,890 to 107,550 lb/ft] along the length of the drift. The rationale for these loads fully manifesting themselves within the first 1,000 years was also provided.

The methodology used to derive the distribution of rock block sizes within the lower lithophysal and middle nonlithophysal rock units was presented in Chapter 4 as well. It was determined from this study that the formation of discrete rock blocks of any consequence within the lower lithophysal rock unit is unlikely because of its highly fractured nature. The analysis of the middle nonlithophysal rock unit, however, indicated that there are rock blocks of sufficient size to cause damage to the drip shield. Some of the rock blocks in the middle nonlithophysal rock unit were calculated to be large enough to cause the drip shield to subsequently impact the waste package. The distribution of rock block sizes within the middle nonlithophysal rock unit is presented in Figures 4-11 and 4-12. These plots indicate that approximately 60 percent of the nonlithophysal rock blocks have a volume less than 1 m^3 [35.3 ft^3], which corresponds to a rock block mass of 2.25 tonne [4,960 lb] {for a rock mass density of 2.25 tonne/m^3 [140 lb/ft^3]}. Twenty-five percent of the rock blocks have a volume of 1 to 2 m^3 [35.3 to 70.6 ft^3] {2.25 to 4.50 tonne [4,960 to 9,920 lb]}, and the remaining 15 percent have a volume greater than 2 m^3 [70.6 ft^3] {4.50 tonne [9,920 lbs]}.

The finite element models used for assessing the potential effects of static rockfall loads on the drip shield were described in Chapter 5. The results obtained from these analyses indicate the drip shield may buckle under static rockfall loads as small as 23 tonne/m [15,460 lb/ft]. Moreover, static rockfall loads sufficient to initiate creep of the drip shield Titanium Grade 7 plate can be as low as 15 tonne/m [10,083 lb/ft] and, for the Titanium Grade 24 bulkhead, 20 tonne/m [13,444 lb/ft]. These threshold loads were found to increase significantly if credit is taken for the structural support provided by the accumulated rockfall rubble that builds up around the drip shield side walls. As a result, a beta function defining the drip shield buckling load was generated (see Figure 5-13). This curve was created assuming the drip shield will not buckle under static rockfall loads less than 25 tonne/m [16,800 lb/ft] and no more than 20 percent of the drip shields will have a buckling load threshold greater than 60 tonne/m [40,330 lb/ft]. In addition, Table 5-6 clearly indicated a correlation between the drip shield buckling load and the maximum von Mises stress within the drip shield plate and bulkhead components. Because the drip shield buckling load is assigned to each spatial grid element using a beta distribution curve as described in Section 5.3.1, the static rockfall load required to generate stresses within the drip shield plate and bulkheads that satisfy the initiation of creep stress threshold was abstracted in terms of the assigned drip shield buckling load.

Chapter 6 presented the concerns regarding potential drip shield and waste package interactions under static rockfall loads. For a contact area between the drip shield bulkhead and waste package outer barrier of 7.6×10^{-4} m^2 [8.18×10^{-3} ft^2], the static rockfall load needed to breach (i.e., exceed the ultimate tensile strength) the Alloy 22 outer barrier is 76.3 tonne/m [51,290 lb/ft]. If the ASME International (2001) Boiler and Pressure Vessel Code failure criterion is used, this threshold load is reduced to 68.7 tonne/m [46,180 lb/ft]. The static rockfall loads needed to breach the waste package will be even smaller if the effective increase in these loads during seismic events is considered. It needs to be recognized, however, that the potential contact area between the drip shield and waste package is likely to increase significantly

because of the large plastic deformation that will be experienced by the Alloy 22 outer barrier when subjected to the surface tractions created by these loads. The contact stress between the waste package and supporting pallet could also exceed the allowable limits for Alloy 22.

There are several important factors that have yet to be adequately considered in the waste package and drip shield interaction analysis: (i) the initial contact area estimated for the drip shield and waste package interaction qualitative assessment can be expected to increase significantly as the outer barrier plastically deforms under the applied load, (ii) the contribution of bending moments to the stress state of the Alloy 22 in the various contact regions created by the overall structural response of the waste package and localized deformations in the immediate areas of the various contact interactions may provide significant contributions to the state of stress in the contact region, and (iii) an angled drip shield bulkhead edge contact orientation may be more appropriate for assessing the potential effects of waste package and drip shield bulkhead interactions. Compared to a drip shield bulkhead and waste package surface-to-surface contact, an angled bulkhead and waste package edge-to-surface contact will require significantly more plastic straining of the outer barrier before any potential state of equilibrium can be achieved. As a result, the edge-to-surface contact is much more likely than the surface-to-surface contact to cause a breach of the waste package outer barrier.

Several abstractions were developed to characterize the response of the drip shield to dynamic rock block impacts (see Chapter 7). Given the rock block mass and impact velocity, the following can be approximated: (i) the maximum deflection of the drip shield, (ii) the maximum von Mises stress and corresponding equivalent plastic strain for the drip shield plate and bulkhead, and (iii) the impact velocity of the drip shield with the waste package for different drip shield and waste package clearances. It was also found that impacts from rock blocks of 8 tonne/m [5,380 lb/ft] or more will likely cause the drip shield to buckle. Smaller rock blocks are likely to cause the drip shield to buckle if they fall from heights greater than the initial 2.1 m [6.89 ft] distance between the drip shield crown and drift roof. The presence of rock rubble was not included in the drip shield and rock block impact analyses because the primary focus of the parametric study was to establish the effects of varying rock block size and rock block impact velocity (i.e., fall height) on the structural behavior of the drip shield. If it is determined that rock block impact with the drip shield is risk significant, additional analyses can be performed to study the potentially beneficial and adverse effects associated with the presence of rock rubble buttressing the drip shield. It is expected that including the presence of rock rubble would reduce the deflection of the drip shield while increasing the likelihood of the Titanium Grade 7 plate being breached for a given rock block impact.

The natural frequencies and mode shapes for the drip shield with varying boundary conditions were presented in Chapter 8. These analyses demonstrated that the type of constraint applied to the drip shield structure will have a significant influence on how it will respond to seismic excitations. For example, the number of modes within the frequency range of a seismic event (i.e., less than or equal to 33 Hz) tend to decrease as additional constraints are added. In the case of the drip shield, the free constraint has 10 mode shapes, the lateral constraint has 5 mode shapes, and the cantilevered constraint has 3 mode shapes that are excited by frequencies less than 33 Hz. None of the 10 free constraint condition mode shapes exhibit a modal participation factor more dominant than the others. The modal participation factors for the lateral constraint condition, however, indicate two of the five mode shapes are more dominant for excitation frequencies below 33 Hz. These mode shapes are the Lateral Wall Zero and Pinch Crown Zero, which respond to excitation in the x-direction (i.e., axial direction). All

three of the mode shapes below 33 Hz for the cantilever constraint condition (i.e., Lateral Wall Zero, Pinch Crown Zero, and Pinch Crown One modes) have a relatively high modal participation factor in either the y- or z-direction (i.e., lateral or vertical direction). Because the drip shield is emplaced as a free-standing structure in the current design of the engineered barrier subsystem, it is not clear how significant higher order effects caused by impact loads arising from the drip shield literally bouncing off the invert foundation or waste package might be during an earthquake.

Only two MECHFAIL spatial grid elements are presently assigned to each subarea of the TPA Version 5.0 beta code. One represents the lower lithophysal rock unit, and the other represents the middle nonlithophysal rock unit. The results obtained for each of these spatial grid elements are weighted using the area percentage of the rock type for the given subarea. A stand-alone version of the MECHFAIL module was used to determine what effect, if any, increasing the number of spatial grid elements per subarea will have on the calculated number of drip shield and drift failures. After 100 realizations, the mean fraction of drip shield and drift failures 520 years into the postclosure period does not appear to be affected by the number of spatial grid elements (see Figures 9-1 and 9-2). The standard deviation for both the calculated mean fraction of drip shield and drift failures, however, is nearly 35 percent when only 2 spatial grid elements per subarea are used. Figure 9-1 indicates that 30 spatial grid elements per subarea are required to reach a converged standard deviation value of approximately 9 percent for the mean fraction of drip shield failures. Similarly, Figure 9-2 shows that 20 spatial grid elements per subarea are required to reach a converged standard deviation value of approximately 12 percent for the mean fraction of drift failures.

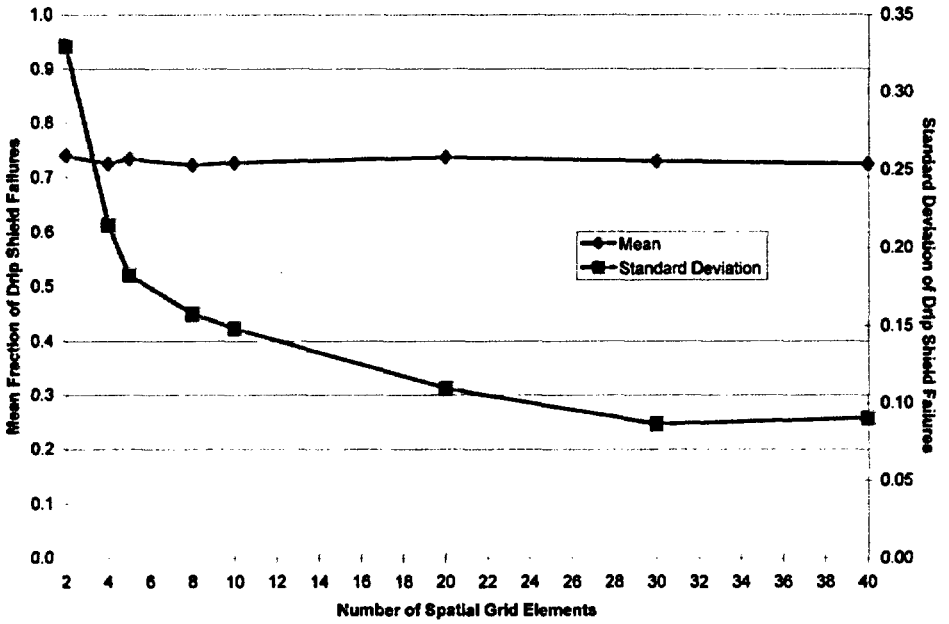

Figure 9-1. Mean Fraction and Standard Deviation of Drip Shield Failures as a Function of the Number of Spatial Grid Elements per Subarea

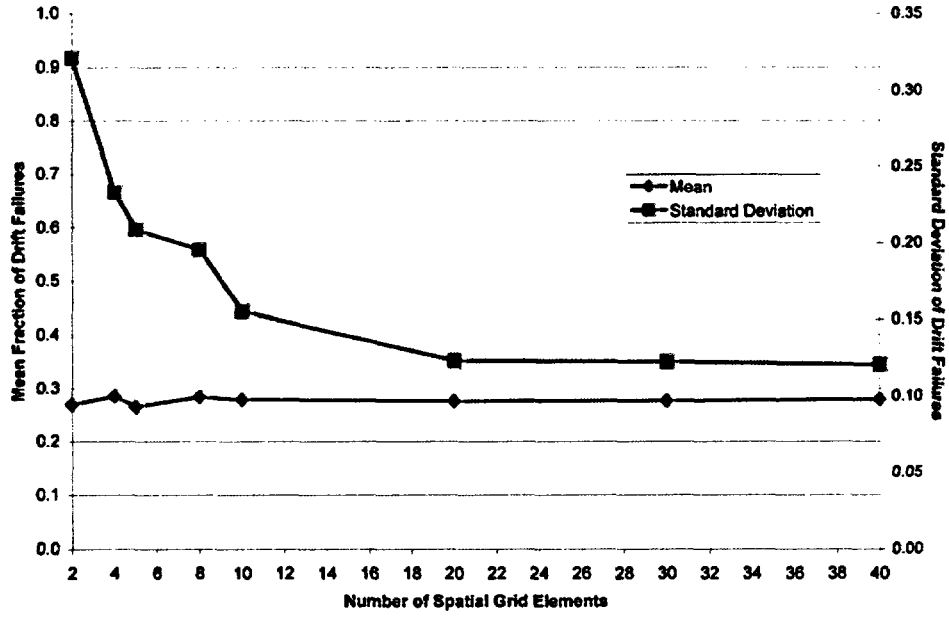

Figure 9-2. Mean Fraction and Standard Deviation of Drift Failures as a Function of the Number of Spatial Grid Elements per Subarea

10 FUTURE WORK

An abstraction for the accumulated rockfall loads and long-term geometry of the emplacement drifts has been completed. This abstraction could be improved, however, if site-specific data for the bulking factors of the lower lithophysal and middle nonlithophysal rock units can be obtained. Unlike the accumulation of static rockfall loads, which are characterized in terms of time degradation parameters and discrete seismic events, dynamic rock block impact loads are correlated with the occurrence of seismic events only. Estimates of the volume of rockfall and, subsequently, the number and size of discrete rock block impacts associated with a given seismic event are based on generic observations and subjective assessments of drift damage. If it can be established that the current methodology used to estimate the volume of rockfall for a given seismic event is reasonably accurate and the effects on the engineered barrier subsystem are negligible, then further refinement of the dynamic rockfall load parameters [i.e., g_o and g_{max} (see Figure 4-14)], may not be necessary. Recall that g_o and g_{max} define the range of mean peak horizontal ground accelerations at which damage to the drift is characterized as being minor (i.e., g_o), and major (i.e., g_{max}). Based on preliminary analyses performed using the MECHFAIL module, failure of the drip shield will likely be dominated by buckling under static rockfall loads. Moreover, dynamic rock block impacts of any significance are only expected to occur in the middle nonlithophysal rock unit, which represents a relatively small percentage of the repository footprint.

The potential failure mechanisms of the drip shield associated with static rockfall loads are buckling and creep. Drip shield failure implies the inability to protect the waste package from rockfall loads and water flow through breaches in the Titanium Grade 7 plate panels. The static rockfall loads needed to cause buckling or initiate creep are strongly dependent on the amount of structural support provided by the rockfall rubble expected to accumulate around the drip shield side walls and the foundational stability provided by the invert. It is not clear at this time if the distributions used for the static rockfall load threshold values for drip shield buckling and creep adequately represent the various effects not explicitly included in the process-level models. For example, the response of the drip shield to the asymmetric buildup of accumulated rockfall rubble or natural load eccentricities may be quite different from the response calculated for the symmetric conditions that were employed in the process level models. Specifically, the symmetric load and boundary conditions applied in the process level models inherently precluded lateral (i.e., horizontal) deflections of the drip shield crown apex. Therefore, the process-level models probably overestimated the structural capabilities of the drip shield when subjected to static rockfall loads because the lateral buckling mode was artificially suppressed. In addition, the drip shield is not bolted, welded, or attached to the carbon steel frame of the invert in any way. As the carbon steel frame corrodes, the foundation of the drip shield would be increasingly compromised and, as a result, the response of the drip shield to rockfall loads (both static and dynamic) could be affected. No attempt was made to assess the potential effects of a degraded carbon steel invert frame in the process-level models. Recognizing that the U.S. Department of Energy (DOE) is presently adding structural reinforcement to its initial design of the drip shield, it is recommended that further analysis of the drip shield subjected to static rockfall loads be postponed until the design is finalized.

Abstractions needed to assess the potential failure of the drip shield and waste package caused by interactions between them under static rockfall, direct seismic shaking, and direct rock block impact load conditions have yet to be developed. The process-level models needed to develop these abstractions are presently under construction.

The various abstractions for the drip shield response to dynamic rock block impacts acceptably represent the failures that may occur from this type of loading condition so long as the drip shield does not interact with the waste package.

Finally, the analyses required to develop abstractions of the potential mechanical failure modes of the various waste forms that DOE plans to emplace at the proposed repository have yet to be initiated. Of particular concern is the potential for spent nuclear fuel assembly cladding failures under seismic conditions. A review of DOE documents that address this topic revealed the full range of potential seismic event magnitudes have not been addressed. Moreover, the analyses used in the DOE documents employ unacceptable assumptions that underestimate the potential for cladding failures under seismic conditions. As a result, it is recommended that work should be pursued in this area to establish a better understanding of the critical parameters and issues regarding this matter.

11 REFERENCES

Ahola, M.P., R. Chen, H. Karimi, S.M. Hsiung, and A.H. Chowdhury. "A Parametric Study of Drift Stability in Jointed Rock Mass. Phase I: Discrete Element Thermal-Mechanical Analysis of Unbackfilled Drifts." CNWRA 96-009. San Antonio, Texas: CNWRA. 1996.

American Society of Civil Engineers. "Seismic Analysis of Safety Related Nuclear Structures and Commentary on Standard for Seismic Analysis of Safety Related Nuclear Structures." ASCE4–98. Reston, Virginia: American Society of Civil Engineers. 1999.

ASM. *Material Properties Handbook: Titanium Alloys.* Materials Park, Ohio: ASM International. 1994.

ASME International. *ASME International Boiler and Pressure Vessel Code.* New York City, New York: ASME International. 2001.

ASTM International. *Standard Specification for Low-Carbon Nickel-Molybdenum-Chromium, Low-Carbon Nickel-Chromium-Molybdenum, Low-Carbon Nickel-Chromium-Molybdenum-Copper, Low-Carbon Nickel-Chromium-Molybdenum-Tantalum, and Low-Carbon Nickel-Chromium-Molybdenum-Tungsten Alloy Plate, Sheet, and Strip.* Philadelphia, Pennsylvania: ASTM International. pp. B575–98. 1998.

Bechtel SAIC Company, LLC. "Resolution Strategy for Geomechanically-Related Repository Design and Thermal-Mechanical Effects (RDTME)." Rev. 00. Las Vegas, Nevada: Bechtel SAIC Company, LLC. 2003.

Brady, B.H.G. and E.T. Brown. *Rock Mechanics for Underground Mining.* London, United Kingdom: George Allen & Unwin. 1985.

CRWMS M&O. "Yucca Mountain Science and Engineering Report." DOE/RW–0539. Las Vegas, Nevada: CRWMS M&O. 2001.

———. "Design Analysis for the Ex-Container Components." ANL–XCS–ME–000001. Rev. 00. Las Vegas, Nevada: CRWMS M&O. 2000a.

———. "Drift Degradation Analysis." ANL–EBS–MD–000027. Rev. 01. Las Vegas, Nevada: CRWMS M&O. 2000b.

———. "Fracture Geometry Analysis for the Stratigraphic Units of the Repository Host Horizon." ANL–EBS–GE–000006. Rev. 00. Las Vegas, Nevada: CRWMS M&O. 2000c.

———. "License Application Design Selection Report." B00000000–01717–4600–00123. Rev. 01. Las Vegas, Nevada: CRWMS M&O. 1999a.

———. "Enhanced Design Alternative II Report." B00000000–01717–5705–00131. Rev. 00. Las Vegas, Nevada: CRWMS M&O. 1999b.

———. "Drip Shields LA Reference Design Feature Evaluation #2." B00000000–01717–2200–00207. Rev. 00. Las Vegas, Nevada: CRWMS M&O. 1999c.

———. "Seismic Ground Motion Hazard Inputs." WP–NEP–99309.T. MOL.19991005.0147. Las Vegas, Nevada: CRWMS M&O. 1999d.

———. "Yucca Mountain Site Geotechnical Report." B00000000–01717–5705–00043. Vol. 1. Rev. 01. Las Vegas, Nevada: CRWMS M&O. 1997a.

———. "Confirmation of Empirical Design Methodologies." BABEE0000–01717–5705–00002. Rev. 00. Las Vegas, Nevada: CRWMS M&O. 1997b.

Das, S.K. "Observations and Classification of Roof Strata Behaviour Over Longwall Coal Mining Panels in India." *International Journal of Rock Mechanics and Mining Sciences.* Vol. 37. pp. 585–597. 2000.

DOE. "Viability Assessment of a Repository at Yucca Mountain." Overview and all five volumes. DOE/RW–0508. Las Vegas, Nevada: DOE, Office of Civilian Radioactive Waste Management. 1998a.

———. "Viability Assessment of a Repository at Yucca Mountain." Vol. 2: Preliminary Design Concept for the Repository and Waste Package. DOE/RW–0508V2. Las Vegas, Nevada: DOE, Office of Civilian Radioactive Waste Management. 1998b.

Dowding, C.H. and A. Rozen. Damage to Rock Tunnels from Earthquake Shaking." *Journal of the Geotechnical Engineering Division, Proceedings of the American Society of Civil Engineers.* 104(GT2). pp. 175–191. 1978.

Gute, G.D., A. Ghosh, S.M. Hsiung, and A.H. Chowdhury. "Assessment of Mechanical Response of Drip Shields Under Repository Environment—Progress Report 2." San Antonio, Texas: CNWRA. 2001.

———. "Assessment of Mechanical Response of Drip Shields Under Repository Environment—Progress Report." San Antonio, Texas: CNWRA. 2000.

Hoek, E. and E.T. Brown. "Practical Estimates of Rock Mass Strength." *International Journal of Rock Mechanics and Mining Sciences.* Vol. 34, No 8. pp. 1,165–1,186. 1997.

———. *Underground Excavations in Rock.* London, United Kingdom: Institution of Mining and Metallurgy. 1980.

Hsiung, S.M., G.H. Shi, and A.H. Chowdhury. "Assessment of Seismically Induced Rockfall in the Emplacement Drifts of the Proposed Repository at Yucca Mountain." San Antonio, Texas: CNWRA. 2001.

Lambe, T.W. and R.V. Whitman. *Soil Mechanics.* New York City, New York: John Wiley and Sons, Inc. 1969.

Manteufel, R.D., M.P. Ahola, D.R. Turner, and A.H. Chowdhury. NUREG/CR–6021, "A Literature Review of Coupled Thermal-Hydrological-Mechanical-Chemical Processes Pertinent to the Proposed High-Level Nuclear Waste Repository at Yucca Mountain." Washington, DC: NRC. July 1993.

Marsal, R.J. "Mechanical Properties of Rockfill." *Embankment-Dam Engineering.* R.C. Hirschfeld and S.J. Poulos, eds. New York City, New York: John Wiley and Sons. 1973.

Neuberger, B.W., C.A. Greene, and G.D. Gute. "Creep Analyses of Titanium Drip Shield Subjected to Rockfall Static Loads in the Proposed Geologic Repository at Yucca Mountain." Scientific Basis for Nuclear Waste Management XXV. B.P. McGrail and G.A. Cragnolino, eds. Symposium Proceedings 713. Pittsburgh, Pennsylvania: Materials Research Society. pp. 97–104. 2002.

NRC. NUREG–1762, "Integrated Issue Resolution Status Report." Washington, DC: NRC. July 2002.

———. "Input to Repository Design and Thermal-Mechanical Effects Issue Resolution Status Report." Rev. 3. Washington, DC: NRC. 2000.

———. NUREG/CR–5440, "Critical Assessment of Seismic and Geomechanics Literature Related to a High-Level Nuclear Waste Underground Repository." Washington, DC: NRC. June 1991.

Ofoegbu, G.I. "Hydrological Implications of Thermally Induced Geomechanical Response at Yucca Mountain, Nevada." Rock Mechanics in the National Interest: Proceedings of the 38th U.S. Rock Mechanics Symposium, Washington, DC, 7–10 July 2001. Lisse, The Netherlands: A.A. Balkema Publishers. pp. 613–619. 2001.

———. "Thermal-Mechanical Effects on Long-Term Hydrological Properties at the Proposed Yucca Mountain Nuclear Waste Repository." CNWRA 2000-03. San Antonio, Texas: CNWRA. 2000.

———. "Variations of Drift Stability at the Proposed Yucca Mountain Repository. Rock Mechanics for Industry." Proceedings of the 37th U.S. Rock Mechanics Symposium 2. B. Amadei, R.L. Kranz, G.A. Scott, and P.H. Smeallie, eds. Rotterdam, Netherlands: A.A. Balkema. pp. 767–773. 1999.

Peng, S.S. and H.S. Chiang. *Longwall Mining.* New York City, New York: John Wiley and Sons. 1984.

U.S. Department of Defense. "Military Handbook: Metallic Materials and Elements for Aerospace Vehicle Structures." MIL–DBK–5H. Washington, DC: U.S. Department of Defense. 1998.

U.S. Geological Survey. "Probabilistic Seismic Hazard Analyses for Fault Displacement and Vibratory Ground Motion at Yucca Mountain, Nevada. Final Report." I.G. Wong and C. Steep, coords. SP32IM3, WBS Number 1.2.3.2.8.3.6. Oakland, California: DOE. 1998.

———. "Geological, Geophysical, and *In-Situ* Stress Investigations in the Vicinity of the Dining Car Chimney, Dining Car/Hybla Gold Drifts, Nevada Test Site." U.S. Geological Survey. Open-File Report 82-137. 1982.

Waiting, D.J., J.A. Stamatakos, D.A. Ferrill, and D.W. Sims. "Methodologies for the Evaluation of Faulting at Yucca Mountain, Nevada." Proceedings of the 10th International High-Level Radioactive Waste Management Conference, Las Vegas, Nevada March 30–April 3, 2003. La Grange Park, Illinois: American Nuclear Society. (cd-rom). 2003.

Wong, F., D. Tennant, J. Isenberg, C. Ludwig, R. Hart, B. Dasgupta, L. Lorig, P. Cundall, and E. Dawson. "Tunnel Size Effects." DNA–TR–91–19. Alexandria, Virginia: Defense Nuclear Agency. 1991.

APPENDIX A

APPLICABLE KEY TECHNICAL ISSUE AGREEMENTS

Table A–1 delineates the various key technical issue agreements between the U.S. Department of Energy (DOE) and U.S. Nuclear Regulatory Commission (NRC) that pertain to the performance assessment of the engineered barrier subsystem when subjected to rockfall and seismic ground motions.

Table A-1. Key Technical Issue Agreements that Pertain to the Performance Assessment of the Engineered Barrier Subsystem when Subjected to Rockfall and Seismic Ground Motions	
Key Technical Issue Agreement Number	**NRC and DOE Agreement**
CLST.1.14	Provide the justification for not including the rockfall effect and dead load from drift collapse on stress corrosion cracking of the waste package and drip shield. DOE will provide the justification for the rockfall and dead-weight effects in the next revision of the stress corrosion cracking Analysis and Model Report (ANL–EBS–MD–000005) prior to license application.
CLST.2.02	Provide the documentation for the point loading rockfall analysis. DOE stated that point loading rockfall calculations will be documented in the next revisions of Analysis and Model Reports ANL–XCS–ME–000001, Design Analysis for the Ex-Container Components, and ANL–UDC–MD–000001, Design Analysis for UCF Waste Packages, both to be completed prior to license application.
CLST.2.06	Provide the technical basis for the mechanical integrity of the inner overpack closure weld. DOE will provide the documentation in Analysis and Model Report, ANL–UDC–MD–000001, Revision 00, Design Analysis for UCF Waste Packages in the next revision, prior to license application.
CLST.2.08	Provide documentation of the path forward items in the "Subissue 2: Effects of Phase Instability of Materials and Initial Defects on the Mechanical Failure and Lifetime of the Containers" presentation, slide 16 [future rockfall evaluations will address: (1) effects of potential embrittlement of waste package closure material after stress annealing due to aging; (2) effects of drip shield wall thinning due to corrosion; (3) effects of hydrogen embrittlement on titanium drip shield; and (4) effects of multiple rock blocks falling on waste package and drip shield; future seismic evaluations will address the effects of static loads from fallen rock on drip shield during seismic events]. DOE stated that the rockfall calculations addressing potential embrittlement of the waste package closure weld and rock falls of multiple rock blocks will be included in the next revision of the Analysis and Model Report, ANL–UDC–MD–000001, Design Analysis for UCF Waste Packages, to be completed prior to License Application. Rock fall calculations addressing drip shield wall thinning due to corrosion, hydrogen embrittlement of titanium, and rock falls of multiple rock blocks will be included in the next revision of the Analysis and Model Report, ANL–XCS–ME–000001, Design Analysis for the Ex-Container Components, to be completed prior to license application. Seismic calculations addressing the load of fallen rock on the drip shield will be included in the next revision of the Analysis and Model Report, ANL–XCS–ME–000001, Design Analysis for the Ex-Container Components, to be completed prior to license application.
CLST.3.10	The agreement addresses CLST Subissues 3 & 4. Provide analysis of the rockfall and vibratory loading effects on the mechanical failure of cladding, as appropriate. DOE stated that the vibratory effects are documented in Sanders et al., 1992, SAND90–2406, A Method For Determining the Spent-Fuel Contribution To Transport Cask Containment Requirements. This will be discussed in the Structural Deformation and Seismicity Key Technical Issue meeting. The analysis of the rockfall effects on the mechanical failure of cladding will be addressed if the agreed to updated rockfall analysis in Subissue #2, Item 8 and Subissue #1, Item 14 demonstrate that the rock will penetrate the drip shield and damage the waste package.

Table A-1. Key Technical Issue Agreements that Pertain to the Performance Assessment of the Engineered Barrier Subsystem when Subjected to Rockfall and Seismic Ground Motions (continued)	
Key Technical Issue Agreement Number	**NRC and DOE Agreement**
RDTME.3.17	Provide the technical basis for effective maximum rock size including consideration of the effect of variation of the joint dip angle. The DOE will provide the technical basis for effective maximum rock size including consideration of the effect of variation of the joint dip angle. This will be documented in revisions to the Drift Degradation Analysis, ANL–EBS–MD–000027, and the Rockfall on Drip Shield, CAL–EBS–ME–000001, expected to be available to NRC in fiscal year 2003.
RDTME.3.19	The acceptability of the process models that determine whether rockfall can be screened out from performance assessment abstractions needs to be substantiated by the DOE by doing the following: (1) provide revised DRKBA analyses using appropriate range of strength properties for rock joints from the Design Analysis Parameters Report, accounting for their long-term degradation; (2) provide an analysis of block sizes based on the full distribution of joint trace length data from the Fracture Geometry Analysis Report for the Stratigraphic Units of the Repository Host Horizon, including small joints trace lengths; (3) verify the results of the revised DRKBA analyses using: (a) appropriate boundary conditions for thermal and seismic loading; (b) critical fracture patterns from the DRKBA Monte Carlo simulations (at least two patterns for each rock unit); (c) thermal and mechanical properties for rock blocks and joints from the Design Analysis Parameters Report; (d) long-term degradation of rock block and joint strength parameters; and (e) site-specific groundmotion time histories appropriate for post-closure period; provide a detailed documentation of the analyses results; and (4) in view of the uncertainties related to the rockfall analyses and the importance of the outcome of the analyses to the performance of the repository, evaluate the impacts of rockfall in performance assessment calculations. DOE believes that the Drift Degradation Analysis is consistent with current understanding of the Yucca Mountain site and the level of detail of the design to date. As understanding of the site and the design evolve, DOE will: (1) provide revised DRKBA analyses using appropriate range of strength properties for rock joints from a design parameters analysis report (or other document), accounting for their long-term degradation; (2) provide an analysis of block sizes based on the full distribution of joint trace length data from the Fracture Geometry Analysis for the Stratigraphic Units of the Repository Host Horizon, ANL–EBS–GE–000006, supplemented by available small joint trace length data; (3) verify the results of the revised DRKBA analyses using: (a) appropriate boundary conditions for thermal and seismic loading; (b) critical fracture patterns from the DRKBA Monte Carlo simulations (at least two patterns for each rock unit); (c) thermal and mechanical properties for rock blocks and joints from a design parameters analysis report (or other document); (d) long-term degradation of joint strength parameters; and (e) site-specific ground motion time histories appropriate for post-closure period. This will be documented in a revision to the Drift Degradation Analysis, ANL–EBS–MD–000027, expected to be available to NRC in fiscal year 2003. Based on the results of the analyses above and subsequent drip shield calculation revisions, DOE will reconsider the screening decision for inclusion or exclusion of rockfall in performance assessment analysis. Any changes to screening decisions will be documented in analyses prior to any potential license application.
SDS.2.04	The approach to evaluate seismic risk, including the assessment of seismic fragility and evaluation of event sequences is not clear to the NRC, provide additional information. DOE believes the approach contained in the Features, Events, and Processes Analysis and Model Report will be sufficient to support the Site Recommendation. The updated Features, Events, and Processes Analysis and Model Report is expected to be available in January 2001.

Table A-1. Key Technical Issue Agreements that Pertain to the Performance Assessment of the Engineered Barrier Subsystem when Subjected to Rockfall and Seismic Ground Motions (continued)	
Key Technical Issue Agreement Number	**NRC and DOE Agreement**
TSPAI.2.02 (Comments 34, 35, 37, 39, 78, and 79)	Provide the technical basis for the screening argument, as summarized in Attachment 2. See Comment # 3, 4, 11, 12, 19 (Parts 1, 2, and 6), 25, 26, 29, 34, 35, 36, 37, 38, 39, 42, 43, 44, 48, 49, 51, 54, 55, 56, 57, 59, 60, 61, 62, 63, 64, 65, 66, 68, 69, 70, 78, 79, J–1, J–2, J–3, J–4, J–7, J–8, J–9, J–10, J–11, J–12, J–13, J–14, J–15, J–17, J–20, J–21, J–22, J–23, J–24, J–25, J–26, and J–27. DOE will provide the technical basis for the screening argument, as summarized in Attachment 2, for the highlighted Features, Events, and Processes. The technical basis will be provided in the referenced Features, Events, and Processes Analysis and Model Report and will be provided to the NRC in fiscal year 2003.
TSPAI.3.06	Provide the technical basis for the methodology used to implement the effects of seismic effects on cladding in revised documentation. DOE will demonstrate that the methodology used to represent the seismic effects of cladding does not result in an underestimation of risk in the regulatory timeframe (ENG2.1.1). DOE will provide the technical basis for the methodology used to implement the effects of seismic effects on cladding in revised documentation. DOE will demonstrate that the methodology used to represent the seismic effects of cladding does not result in an underestimation of risk in the regulatory timeframe in Total-system Performance Assessment-License Application. The documentation is expected to be available to NRC in fiscal year 2003.
GEN.1.01 (Comment 3)	For NRC comments 3, 5, 8, 9, 10, 12, 13, 15, 16, 18, 21, 24, 27, 36, 37, 41, 42, 45, 46, 50, 56, 64, 69, 75, 78, 81, 82, 83, 93, 95, 96, 97, 98, 102, 103, 104, 106, 109, 110, 111, 113, 116, 118, 119, 120, 122, 123, 124, and 126, DOE will address the concern in the documentation for the specific Key Technical Issue agreement identified in the DOE response (Attachment 2). The schedule and document source will be the same as the specific Key Technical Issue agreement.